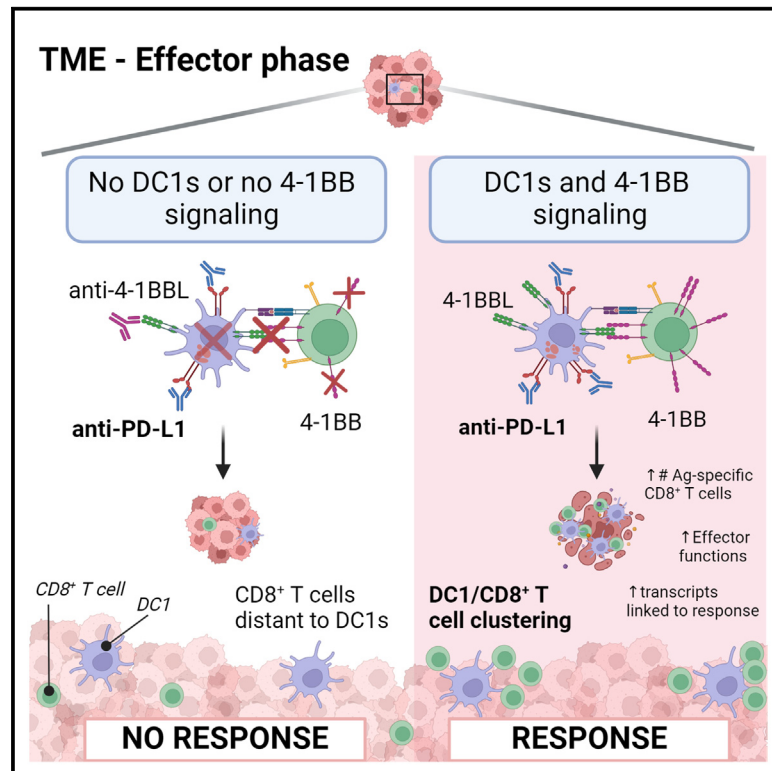


Batf3⁺ DCs and the 4-1BB/4-1BBL axis are required at the effector phase in the tumor microenvironment for PD-1/PD-L1 blockade efficacy

Graphical abstract



Authors

Andrea Ziblat, Brendan L. Horton, Emily F. Higgs, ..., YuanYuan Zha, Randy F. Sweis, Thomas F. Gajewski

Correspondence

tgajewsk@bsd.uchicago.edu

In brief

Ziblat et al. demonstrate that Batf3⁺ dendritic cells (DC1s) are needed within the tumor for efficacy of PD-1/PD-L1 blockade. Mechanistically, they show that DC1s deliver positive signals through 4-1BB/4-1BBL for the reinvigoration of CD8⁺ T cells once PD-1/PD-L1 is blocked and that DC1-CD8 clustering correlates with anti-PD-1 clinical efficacy.

Highlights

- DC1s are needed in the TME for PD-1/PD-L1 blockade efficacy
- Anti-PD-L1-induced CD8⁺ T cell reinvigoration in the TME is 4-1BB/4-1BBL dependent
- DC1/CD8⁺ T cell clustering is associated with clinical response to PD-1 blockade
- CD8⁺ T cell proximity to DC1 is associated with transcriptomics linked to treatment response



Article

Batf3⁺ DCs and the 4-1BB/4-1BBL axis are required at the effector phase in the tumor microenvironment for PD-1/PD-L1 blockade efficacy

Andrea Ziblat,¹ Brendan L. Horton,¹ Emily F. Higgs,¹ Ken Hatogai,¹ Anna Martinez,¹ Jason W. Shapiro,² Danny E.C. Kim,¹ YuanYuan Zha,³ Randy F. Sweis,⁴ and Thomas F. Gajewski^{1,4,5,*}

¹Department of Pathology, Section of Hematology/Oncology, University of Chicago, Chicago, IL 60637, USA

²Center for Research Informatics, University of Chicago, Chicago, IL 60637, USA

³Human Immunological Monitoring Facility, University of Chicago, Chicago, IL 60637, USA

⁴Department of Medicine, University of Chicago, Chicago, IL 60612, USA

⁵Lead contact

*Correspondence: tgajewski@bsd.uchicago.edu

<https://doi.org/10.1016/j.celrep.2024.114141>

SUMMARY

The cellular source of positive signals that reinvigorate T cells within the tumor microenvironment (TME) for the therapeutic efficacy of programmed death-1 (PD-1)/programmed death-ligand 1 (PD-L1) blockade has not been clearly defined. We now show that Batf3-lineage dendritic cells (DCs) are essential in this process. Flow cytometric analysis, gene-targeted mice, and blocking antibody studies revealed that 4-1BBL is a major positive co-stimulatory signal provided by these DCs within the TME that translates to CD8⁺ T cell functional reinvigoration and tumor regression. Immunofluorescence and spatial transcriptomics on human tumor samples revealed clustering of Batf3⁺ DCs and CD8⁺ T cells, which correlates with anti-PD-1 efficacy. In addition, proximity to Batf3⁺ DCs within the TME is associated with CD8⁺ T cell transcriptional states linked to anti-PD-1 response. Our results demonstrate that Batf3⁺ DCs within the TME are critical for PD-1/PD-L1 blockade efficacy and indicate a major role for the 4-1BB/4-1BB ligand (4-1BBL) axis during this process.

INTRODUCTION

Programmed death-1 (PD-1)/programmed death-ligand 1 (PD-L1) blockade has shown clinical benefit across many cancer types.^{1,2} However, many patients are resistant to treatment and some responding patients eventually relapse.³ Previous work has indicated that anti-PD-1 responders have a higher number of CD8⁺ T cells in the tumor microenvironment (TME) at baseline and that tumor-infiltrating T cells expand following treatment compared to non-responders.^{4,5} However, the cellular and molecular interactions driving this and the expression of T cell activation genes within the TME are not clearly defined. Understanding the dynamics of cell-cell interactions that might be operational in the TME at the time of PD-1/PD-L1 blockade could help define the requirements for restoration of T cell function and provide novel insights toward designing new interventions to expand efficacy further.

Preclinical mouse studies have demonstrated that the generation of a T cell-inflamed TME depends on dendritic cells (DCs). DCs are comprised of distinct subpopulations, but they have been mostly defined as plasmacytoid DCs (pDCs) and conventional DCs (cDCs).⁶ cDCs are subdivided into DC1s, which require Batf3 and IRF8 transcription factors for their development, and DC2s which require IRF4.^{7,8} In mice, DC1s express surface CD8 α and/or CD103 molecules and excel at cross-pre-

senting antigen (Ag) to CD8⁺ T cells, while DC2s mainly activate CD4⁺ T cells.⁶ Importantly, DC1s have been shown to be critical at both the afferent and the efferent stages of anti-tumor immunity. Batf3-deficient mice show poor priming of tumor Ag-specific CD8⁺ T cells in the tumor-draining lymph nodes (tdLNs), indicating a key role for DC1s in the initiation of anti-tumor T cell responses.^{9,10} In a second stage, DC1s within the TME have been shown to contribute to the recruitment of CD8⁺ effector T cells through the production of the chemokines CXCL9 and CXCL10.^{11–13}

While it has been shown that DC1s are necessary for PD-1/PD-L1 blockade efficacy in mouse models, the stages within the cancer-immunity cycle in which these DCs are necessary for treatment to work have not been thoroughly investigated. The requirement for DC1s for PD-1/PD-L1 blockade efficacy was demonstrated by the use of Batf3 knockout (KO) mice or by depleting DC1s at an early time point of tumor development.^{14–17} These results have indicated a critical role for DC1s during the priming phase, but also at the level of the target tissue, for effector T cell migration into the TME. However, since PD-1/PD-L1 blockade treatment is given to patients when tumors are already established, it has become critical to investigate whether DC1s are also necessary at a third stage of the anti-tumor immune response as a potential source of positive signals within the TME for CD8⁺ T cell reinvigoration



at the moment of PD-L1/PD-1 interruption via monoclonal antibody (mAb) blockade.

RESULTS

To investigate the need for DCs at the effector phase of the anti-tumor immune response within the TME for anti-PD-L1 efficacy, we used the B16-SIY melanoma model^{18,19} and CD11c_Diphtheria Toxin Receptor (DTR)_EGFP bone marrow (BM) chimeras to deplete CD11c⁺ cells after T cell priming and migration to the tumor occurred but prior to anti-PD-L1 treatment. As shown in the experimental design (Figure 1A), we waited 7 days after tumor injection for the establishment of a T cell-inflamed TME, and from this day until the end of the experiment, CD11c⁺ cells were depleted or not with diphtheria toxin (DT). To focus on the role of CD11c⁺ cells in the PD-L1-blockade-induced reinvigoration of dysfunctional CD8⁺ T cells already present in the TME, and not in the priming and recruitment of new T cell clones, we blocked new T cell entry into the tumor starting on day 7 after tumor inoculation with fingolimod (FTY720, a functional antagonist of the S1P1 receptor that prevents T cell egress from LNs). Then, anti-PD-L1 treatment was initiated. Of note, before tumor injection, the percentage of hematopoietic chimerism was evaluated and was always above 90% donor origin (Figure S1A), and FTY720 treatment efficacy was confirmed by evaluating the frequency of CD3⁺ T cells in peripheral blood of mice at endpoint (Figure S1B). As expected, anti-PD-L1 was therapeutic in this model (Figure 1B), relying on T cells already present within the tumor site, as we have shown previously.²⁰ However, this therapeutic effect was lost in the group of mice depleted of CD11c⁺ cells after the priming and recruitment of T cells into the TME occurred and just before anti-PD-L1 treatment (Figure 1B). Of note, in control mice, we observed a significant increase in the number of CD11c⁺EGFP⁺ cells per gram of tumor upon anti-PD-L1 treatment, which was not seen with DT treatment, as expected (Figures S1C and S1D). We further investigated intratumoral DC accumulation upon PD-L1/PD-1 blockade by analyzing the different DC subpopulations: pDCs, CD103⁺ DCs (DC1s), and CD11b⁺CD103[−] DCs (DC2s) (gating strategy depicted in Figure S1E). Notably, there was a significant increase in the number of DC1s and DC2s per gram of tumor upon anti-PD-L1 treatment in control mice, along with a trend toward increases in pDCs (Figures S1F, S1G, and S1H, respectively), and the numbers of the three types of DCs were substantially reduced when CD11c⁺ cells were depleted. In addition, we studied the effect of anti-PD-L1 treatment on the number of T cells in the presence or absence of CD11c⁺ cells (gating strategy shown in Figure S1I). Strikingly, while we observed the expected increase in the number of Ag-specific CD8⁺ T cells (CD8⁺SIY⁺) per gram of tumor following anti-PD-L1 treatment in control mice, this effect was lost when DCs were depleted (Figure 1C). Accordingly, we observed a trend toward an anti-PD-L1-induced increased proliferation of CD8⁺SIY⁺ T cells, and the percentage of proliferating cells upon treatment was significantly decreased in the absence of DCs (Figure 1D). Interestingly, while we did not observe significant differences in the percentage of apoptotic cells between the conditions (Figure 1E), there was a DC-dependent significant

increase in the proliferating-to-apoptotic cell ratio with anti-PD-L1 treatment (Figure 1F). We also detected an increased number of CD4⁺ regulatory T cells (Tregs) per gram of tumor with treatment that did not occur in the absence of DCs (Figure 1G). This could be explained by our previous work showing that CD8⁺ T cells in the TME are largely responsible for the local accumulation of Tregs.²¹ Combining these data into one parameter, we observed a significant increase in the ratio of Ag-specific CD8⁺ T cells to Tregs with anti-PD-L1 treatment that did not occur in the absence of DCs (Figure 1H). A high CD8⁺ T cell-to-Treg ratio has been shown to be associated with favorable prognosis in various cancer contexts and also with checkpoint blockade efficacy.^{22,23} Together, these results indicate that CD11c⁺ DCs are needed in the TME at the effector phase for anti-PD-L1 efficacy because they promote the accumulation of Ag-specific CD8⁺ T cells following treatment by increasing their proliferation-to-apoptotic ratio.

Given the previous evidence indicating a particular requirement for DC1s for anti-tumor CD8⁺ T cell responses, we decided to analyze whether DC1s are also the specific type of CD11c⁺ cell required in the TME for checkpoint blockade efficacy. Supporting this notion, we observed a significant correlation between the numbers of CD103⁺ DCs and CD8⁺SIY⁺ T cells in the anti-PD-L1-treated tumors from chimeric mice that was also inversely associated with tumor weights at the experimental endpoints (Figure 1I). To explore necessity, we generated mixed BM chimeras of CD11c_DTR_EGFP BM plus wild-type (WT) BM and CD11c_DTR_EGFP BM plus Batf3 KO BM (experimental design shown in Figure 2A). The percentage of chimerism in each group was evaluated prior to tumor injection and was close to 50% of each donor BM (Figure S2A). From day 7 of tumor injection, after the priming and recruitment of CD8⁺ T cells into the tumor occurred, new T cell entry to the tumor was prevented with FTY720, and mice were treated with DT to deplete the CD11c⁺ cells from the CD11c_DTR_EGFP BM. Because of the mixed BM chimera design, starting on day 7 of tumor injection, half of the mice continued to have WT CD11c⁺ DCs (and any other CD11c⁺ cell), but the other half lacked only Batf3⁺ DCs. Strikingly, while the first group of mice showed significant tumor growth control with anti-PD-L1 treatment, immunotherapy efficacy was lost in the mice that lacked Batf3⁺ DCs while having the rest of CD11c⁺ cells at the effector phase (Figure 2B). To study how the absence of Batf3⁺ DCs affects anti-PD-L1 efficacy, and after confirming FTY720 efficacy (Figure S2B), we analyzed the numbers of other immune cells infiltrating the tumor. With the gating strategy depicted in Figure S2C, we observed a slight increase in the number of pDCs per gram of tumor in the absence of Batf3⁺ DCs, but their number was not affected by immunotherapy (Figure S2D). Also, there was a trend for an increased number of DC2s per gram of tumor upon anti-PD-L1 that did not reach statistical significance (Figure S2E). However, we observed again an increased number of DC1s per gram of tumor with anti-PD-L1 treatment that, as expected, did not occur in the group of mice with Batf3 KO BM (Figure S2F). Noteworthy, we also observed an anti-PD-L1-induced increased number of DC1s in B6 mice without FTY720 treatment, confirming that the result was not a singularity of the model (Figure S2G).

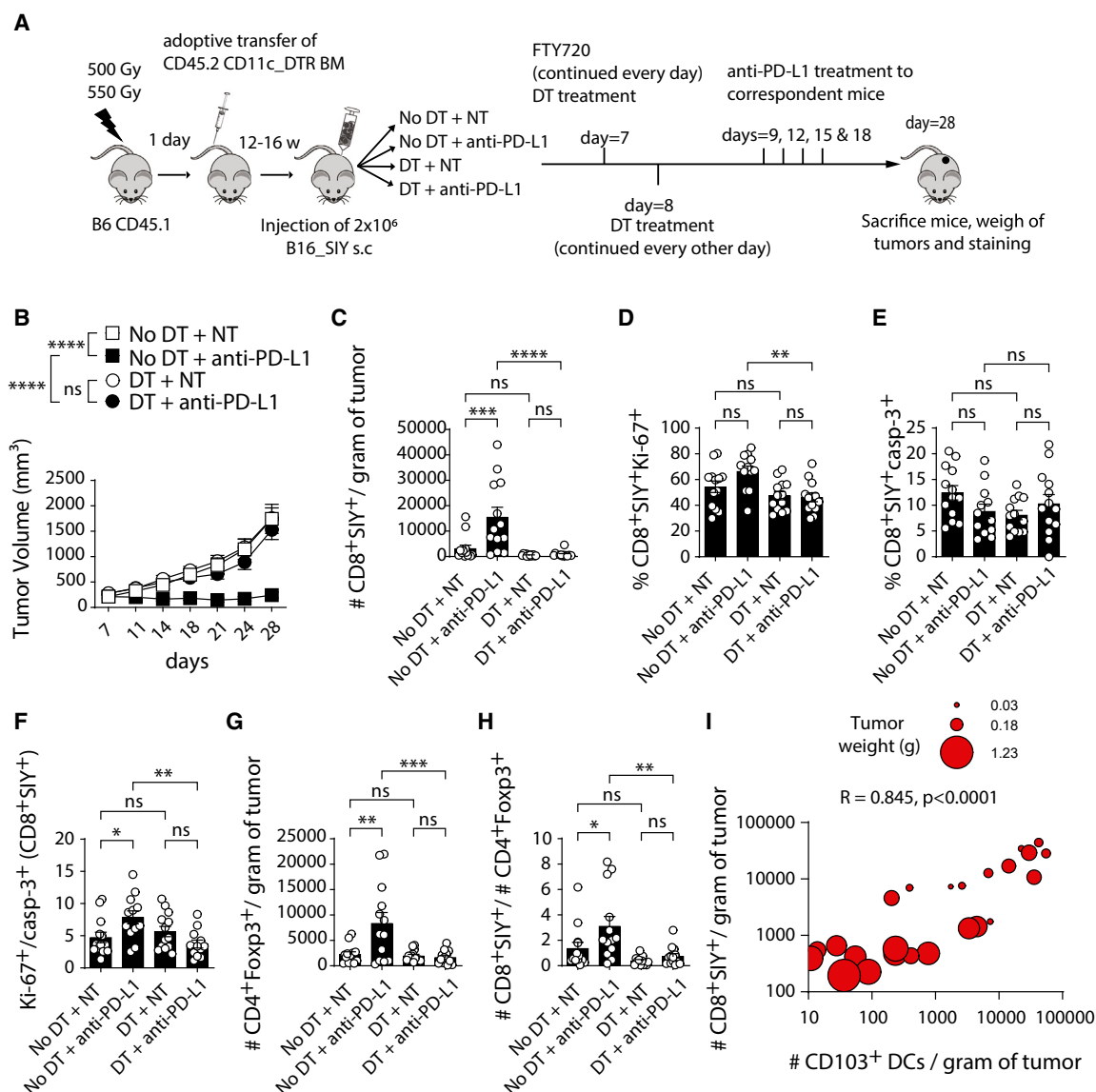


Figure 1. CD11c⁺ DCs are necessary at the effector phase of the anti-tumor immune response for anti-PD-L1 treatment efficacy

(A) CD11c⁺_DTR chimeric mice experimental design.

(B) Tumor growth curves of chimeric mice injected with B16_S1Y cells.

(C) Number of CD8⁺SIY⁺ T cells per gram of tumor in each group.

(D and E) Percentage of proliferating (D) or apoptotic (E) CD8⁺SIY⁺ T cells in each group.

(F) CD8⁺SIY⁺ T cell proliferation-to-apoptotic ratio in each group.

(G and H) Number of Foxp3⁺CD4⁺ T cells per gram of tumor (G) and CD8⁺SIY⁺ T cell-to-Foxp3⁺ CD4⁺ T cell ratio (H) in each group, $n \geq 12$ per group.

(I) Correlation between the numbers of DC1s and SIY⁺CD8⁺ T cells in the anti-PD-L1-treated tumors from chimeric mice, and its association to tumor weight at the end of the experiment. Each dot on the graph represents one mouse, and it is sized according to tumor weight, $n = 26$.

Two independent experiments in all graphs. Bar graphs represent the mean values of the indicated data points, and the error bars represent SEM. ns, not significant; * $p < 0.05$, ** $p < 0.01$, *** $p < 0.001$, and **** $p < 0.0001$. Two-way ANOVA with Tukey's post-test (B), one-way ANOVA with Bonferroni's post-test (C–H), and Spearman's correlation (I) were used for statistical analysis.

Moreover, we observed that upon anti-PD-L1 treatment, there was a significant increase in the number of CD8⁺SIY⁺ T cells per gram of tumor and an increase in the CD8⁺SIY⁺ T cell-to-Treg ratio that failed to occur in the absence of Batf3⁺ DCs (Figures 2C and 2D, respectively). In addition, similarly to the CD11c_DTR_EGFP BM chimeras, we observed a trend to-

ward an anti-PD-L1-induced increased proliferation of Ag-specific CD8⁺ T cells, and the percentage of proliferating cells upon treatment was significantly decreased in the absence of Batf3⁺ DCs (Figure 2E).

Next, to extend these results, we repeated the experiments with the MC38.S1Y colon adenocarcinoma tumor model.

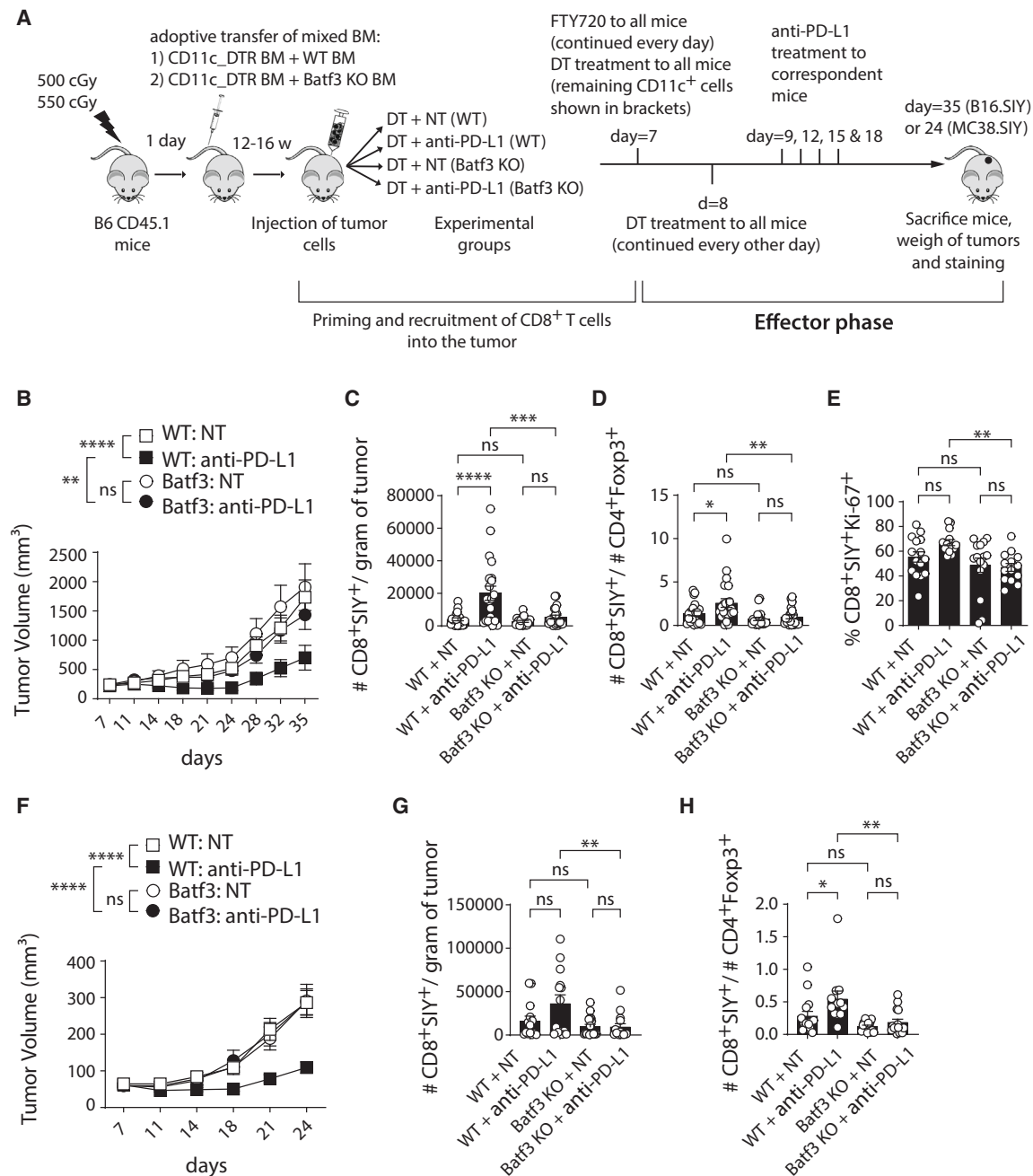


Figure 2. Batf3⁺ DCs are necessary within the TME at the effector phase of the anti-tumor response for anti-PD-L1 treatment efficacy and Ag-specific CD8⁺ T cell accumulation

(A) Mixed BM chimera experimental design.

(B) Tumor outgrowth curves of B16.SIY cells injected in mixed BM chimeras, $n \geq 23$ per group.

(C) Number of CD8⁺SIY⁺ T cells per gram of tumor in each group, $n \geq 20$ per group.

(D) CD8⁺SIY⁺ T cell-to-Foxp3⁺ T cell ratio in each group, $n \geq 21$ per group.

(E) Percentage of proliferating CD8⁺SIY⁺ T cells in each group, $n \geq 13$ per group.

(F) Tumor outgrowth curves of MC38.SIY cells injected in mixed BM chimeras, $n \geq 16$ per group.

(G) Number of CD8⁺SIY⁺ T cells per gram of tumor in each group, $n \geq 14$ per group.

(H) CD8⁺SIY⁺ T cell-to-Foxp3⁺ T cell ratio in each group, $n \geq 12$ per group.

Three independent experiments for (B)–(D) and two independent experiments for (E)–(H). Bar graphs represent the mean values of the indicated data points, and the error bars represent SEM. ns, not significant; * $p < 0.05$, ** $p < 0.01$, *** $p < 0.001$, and **** $p < 0.0001$. Outliers were removed using GraphPad Prism with the robust regression followed by outlier identification (ROUT) method with a $Q = 0.1\%$. Two-way ANOVA with Tukey's post-test (B and F) and one-way ANOVA with Bonferroni's post-test (C–E, G, and H) were used for statistical analysis.

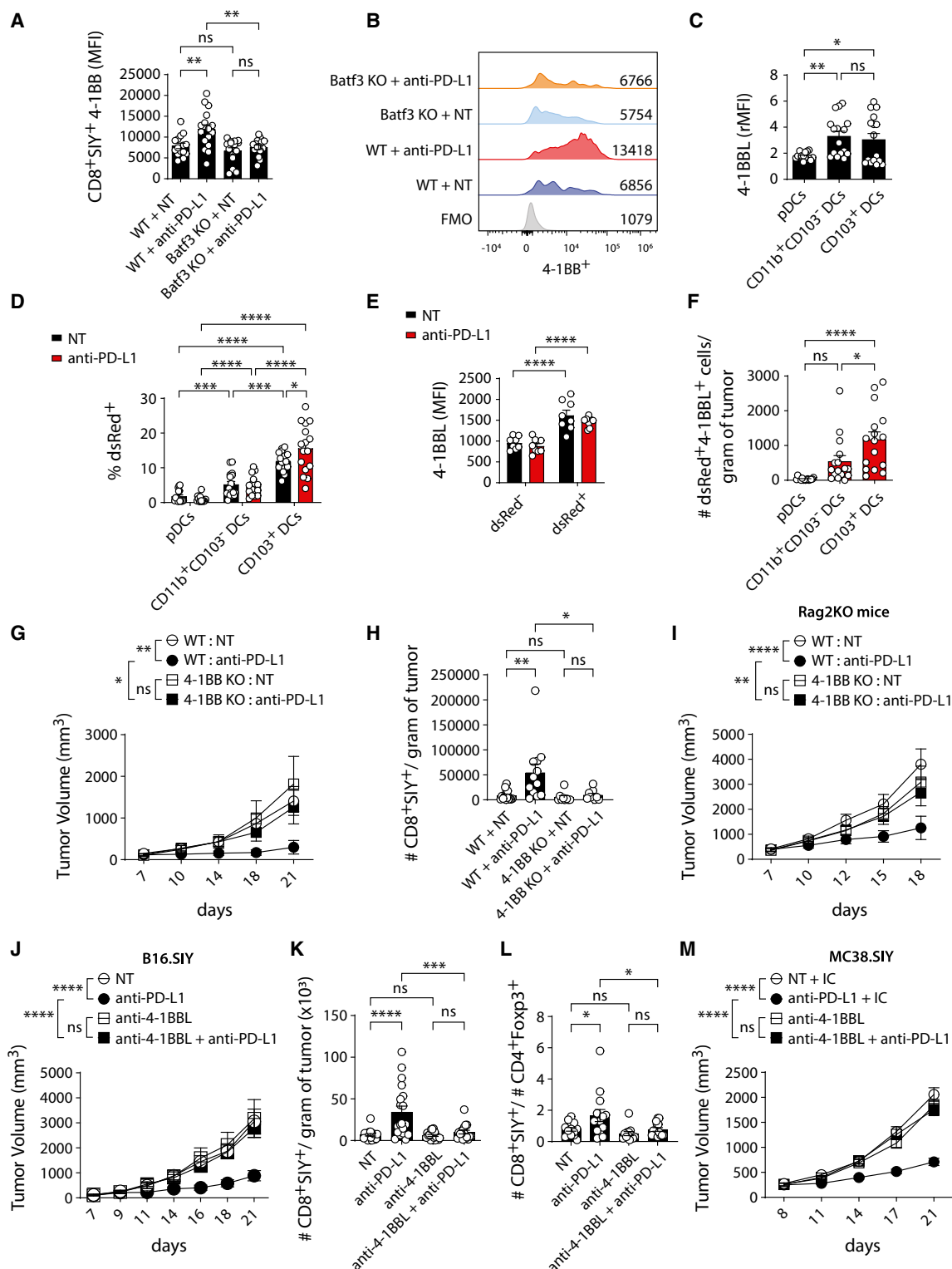


Figure 3. Batf3⁺ DCs and Ag-specific CD8⁺ T cells communicate in the TME through the 4-1BB/4-1BBL axis for anti-PD-L1-induced tumor growth control

(A) 4-1BB expression on CD8⁺SIY⁺ T cells in each condition. Experimental design is shown in Figure 2A, $n \geq 15$ per group.

(B) Representative histograms. Mean fluorescence intensity (MFI) values are shown inside the graph.

(legend continued on next page)

Similarly, chimeric mice that lacked Batf3⁺ DCs at the effector phase were not able to control tumor growth upon anti-PD-L1 treatment (Figure 2F). In addition, there was a significantly lower number of CD8⁺SIY⁺ T per gram of tumor (Figure 2G) and a lower CD8⁺SIY⁺ T cell-to-Treg ratio (Figure 2H) in the mice that lacked Batf3⁺ DCs compared to the group of mice that had Batf3⁺ DCs during anti-PD-L1 treatment. These results suggest that Batf3⁺ DCs, among the CD11c⁺ cells, are the main drivers of anti-PD-L1 efficacy within the TME and act by inducing Ag-specific CD8⁺ T cell accumulation at the effector phase of the anti-tumor immune response once PD-1/PD-L1 interactions are inhibited.

Understanding the signals provided by the DC1s to the Ag-specific CD8⁺ T cells that promote tumor control upon anti-PD-L1 treatment may allow for the design of new interventions directly targeting CD8⁺ T cells. Therefore, we decided to investigate how Batf3⁺ DCs and Ag-specific CD8⁺ T cells communicate upon treatment. To this end, we evaluated the expression of several functionally relevant receptors on the CD8⁺SIY⁺ T cells. We observed that while there were no changes in LAG-3, PD-1, or Tim-3 with anti-PD-L1 treatment (Figures S3A, S3B, and S3C, respectively), there was an increased expression of 4-1BB that did not occur in the absence of Batf3⁺ DCs (Figures 3A and 3B). Of note, the anti-PD-L1-induced increased expression of 4-1BB was also observed at day 15 of tumor injection (Figure S3D) and also without FTY720 treatment (Figure S3E).

To explore further, we evaluated 4-1BBL expression on DCs 1 day after the first dose of anti-PD-L1 (gating strategy shown in Figure S2C) and observed that both DC1s and DC2s expressed higher levels of 4-1BBL than pDCs (Figure 3C). We expect that the functionally relevant Ag-presenting cells within the TME should be those that take up antigen for cognate interaction with the CD8⁺ T cells at the moment of their anti-PD-L1-mediated reinvigoration. Therefore, taking advantage of dsRed expression by tumor cells in our model, we analyzed the acquisition of tumor-derived material by tumor-infiltrating DCs. Interestingly, we found that a significantly higher percentage of DC1s acquired dsRed compared to pDCs and DC2s at baseline, and this percentage was significantly increased only in the DC1s cells upon anti-PD-L1 treatment (Figures 3D and S3F). Interestingly, DC1s that acquired tumor-derived material also expressed

higher amounts of 4-1BBL (Figure 3E). Furthermore, we observed that in the TME of mice treated with anti-PD-L1, there was a higher number of dsRed⁺4-1BBL⁺ DC1s per gram of tumor than dsRed⁺4-1BBL⁺ pDCs and dsRed⁺4-1BBL⁺ DC2s (Figure 3F). These results, together with the mixed BM chimera results, which showed that even in the presence of DC2s and pDCs (which express 4-1BBL), anti-PD-L1 treatment was not effective if the mice lacked DC1s, suggest a relevant role for 4-1BBL expression on DC1s for efficacy.

To determine whether the 4-1BB/4-1BBL axis was functionally involved in anti-PD-L1 efficacy, we utilized 4-1BB KO mice as hosts. In fact, anti-PD-L1 failed to result in tumor growth control in 4-1BB KO mice compared to control mice (Figure 3G). Accordingly, CD8⁺SIY⁺ T cells did not expand in the TME after treatment (Figure 3H). Next, to confirm that 4-1BB expression was necessary on immune cells for anti-PD-L1 efficacy, we adoptively transferred 4-1BB KO or WT splenocytes into Rag2 KO mice. We observed that the group of mice reconstituted with 4-1BB KO immune cells were unable to control tumor growth with anti-PD-L1 treatment compared to mice that received WT immune cells (Figure 3I). We also analyzed the requirement for 4-1BBL in anti-PD-L1 efficacy, in this case focusing on the effector phase. To do so, we prevented new T cell entry to the tumor with FTY720 after tumor establishment and used a blocking anti-4-1BBL mAb. We observed that while mice treated with anti-PD-L1 were able to control tumor growth and increase the CD8⁺SIY⁺ T cells per gram of tumor and the CD8⁺SIY⁺ T cell-to-Treg ratio as usual, mice treated simultaneously with anti-PD-L1 plus anti-4-1BBL mAb failed to do so (Figures 3J, 3K, and 3L, respectively). Interestingly, the anti-PD-L1-induced increased proliferating-to-apoptotic ratio in the Ag-specific CD8⁺ T cells that did not occur in the absence of CD11c⁺ cells (Figure 1F) was also prevented in the presence of 4-1BBL-blocking mAb (Figure S3G). In the second tumor model (MC38.SIY), anti-PD-L1 also lost efficacy when 4-1BBL was simultaneously blocked (Figure 3M).

To investigate whether the 4-1BB/4-1BBL axis was also affecting the Ag-specific CD8⁺ T cell functionality in the TME, we evaluated the expression of the degranulation marker CD107a. We observed an increased percentage of CD8⁺SIY⁺ T cells that degranulated with anti-PD-L1 treatment in WT

(C) Relative 4-1BBL expression, expressed as relative MFI (rMFI = MFI/MFI of FMO) on pDCs, DC1s, and DC2s at day 9 of tumor injection, 1 day after one dose of anti-PD-L1 treatment. Gating strategy described in Figure S2C, *n* = 16 per group.

(D) Percentage of pDCs, DC1s, and DC2s that acquired dsRed (tumor Ag) with and without anti-PD-L1 treatment, *n* = 16 per group.

(E) Expression levels of 4-1BBL on DC1s that did or did not acquire dsRed. One of two independent experiments is shown, *n* = 8 per group.

(F) Number of pDCs, DC1s, and DC2s per gram of tumor that acquired dsRed and express 4-1BBL upon anti-PD-L1 treatment, *n* = 16 per group.

(G) Tumor growth curves of B16-SIY cells injected in WT or 4-1BB KO mice and treated or not with anti-PD-L1, *n* ≥ 10 per group.

(H) Number of CD8⁺SIY⁺ T cells per gram of tumor in each group at day 21 after tumor injection, *n* ≥ 9 per group.

(I) Tumor growth curves of B16-SIY cells injected in Rag2 KO mice reconstituted with WT or 4-1BB KO splenocytes and treated or not with anti-PD-L1, *n* = 13 per group.

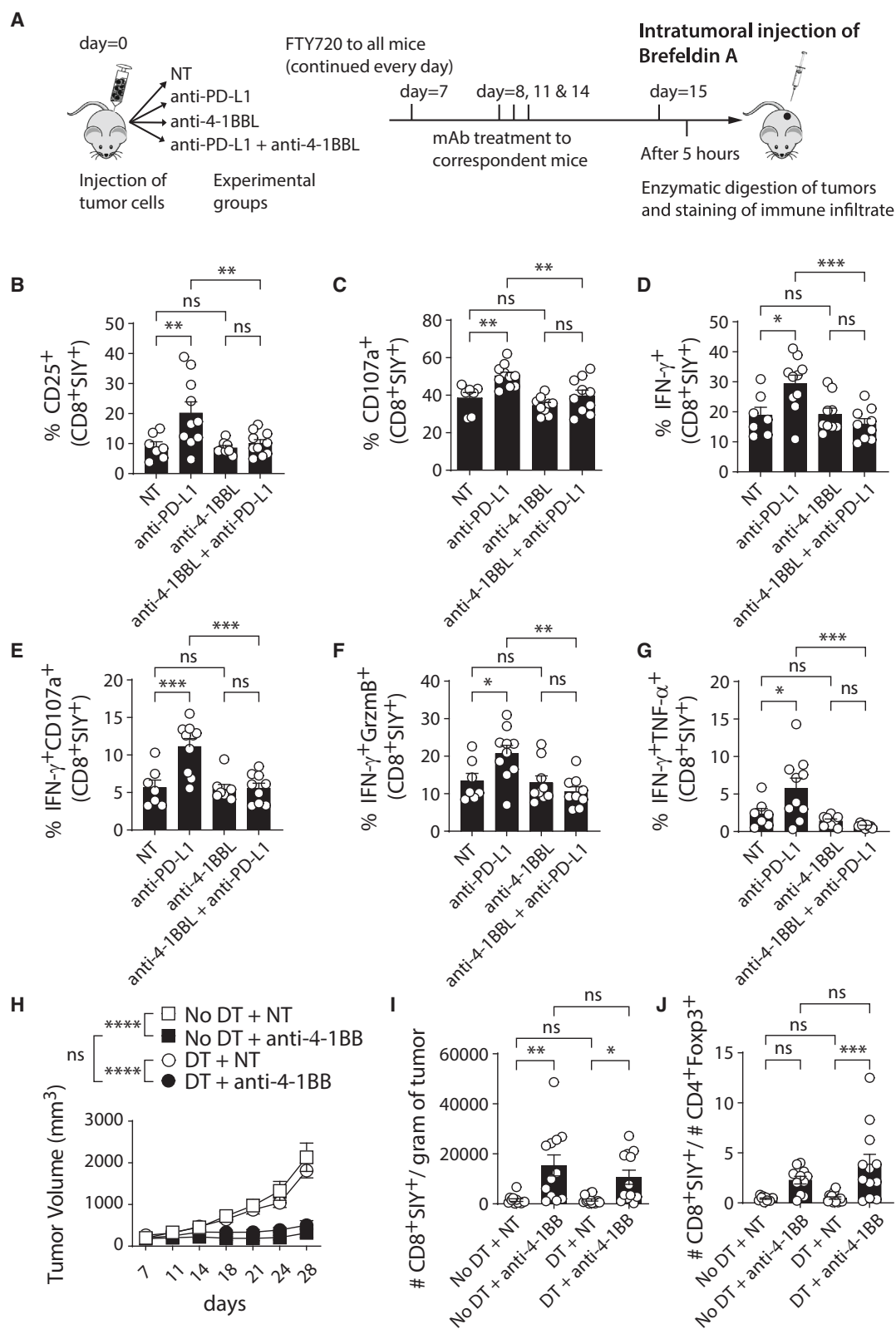
(J) Tumor growth curves of B16-SIY cells injected in C57BL/6 mice, treated every day with FTY720 from day 7 of tumor injection, and treated with or without anti-PD-L1 mAb in the absence or presence of anti-4-1BBL-blocking mAb, *n* ≥ 9 per group.

(K) Number of CD8⁺SIY⁺ T cells per gram of tumor at day 15 after tumor injection. Mice were treated as in (J) but analyzed after 3 doses of mAb treatments. Three independent experiments, *n* ≥ 17 per group.

(L) CD8⁺SIY⁺ T cell-to-Foxp3⁺ T cell ratio in each group of mice treated as in (K), *n* ≥ 12 per group.

(M) Tumor growth curves of MC38.SIY cells injected in C57BL/6 mice and treated as in (J), *n* ≥ 15 per group.

Two independent experiments in all graphs unless stated otherwise. Bar graphs represent the mean values of the indicated data points, and the error bars represent SEM. ns, not significant; **p* < 0.05, ***p* < 0.01, ****p* < 0.001, and *****p* < 0.0001. One-way ANOVA with Bonferroni's post-test (A, C, F, H, K, and L), two-way ANOVA with Bonferroni's post-test (D and E), and two-way ANOVA with Tukey's post-test (G, I, J, and M) were used for statistical analysis.



(legend on next page)

mice, and this effect did not occur in 4-1BB KO mice (Figure S4A). In addition, in B6 mice injected with MC38.SIY and treated with FTY720 starting on day 7 of tumor injection, there was an anti-PD-L1-induced increased frequency of CD8⁺SIY⁺CD107a⁺ T cells, and this effect failed to occur when 4-1BBL was simultaneously blocked (Figure S4B). To further investigate the functionality of the cells under these conditions, we repeated the experiment with B16.SIY tumor inoculation, and we injected brefeldin A intratumorally (experimental design depicted in Figure 4A). Interestingly, we observed an increased percentage of activated Ag-specific CD8⁺ T cells (CD25⁺, Figure 4B) and an increased frequency of CD8⁺SIY⁺ T cells that degranulated (CD107a⁺, Figure 4C) and produced interferon (IFN)- γ (Figure 4D) upon anti-PD-L1 treatment that did not occur when 4-1BBL was simultaneously blocked. Moreover, when mice were simultaneously treated with anti-PD-L1 plus anti-4-1BBL mAb, there was a significant reduction in the percentage of CD8⁺SIY⁺ T cells that produced interleukin-2 (Figure S4C) and tumor necrosis factor α (TNF- α) (Figure S4D) compared to anti-PD-L1 alone. Furthermore, blocking of 4-1BBL prevented the anti-PD-L1-induced increase in the percentage of polyfunctional Ag-specific CD8⁺ T cells (Figures 4E–4G). Altogether, these results suggest that Batf3⁺ DCs are needed at the effector phase for anti-PD-L1 efficacy because of the positive signals that these cells provide to the Ag-specific CD8⁺ T cells through the 4-1BB/4-1BBL axis, both for their expansion and for their functional reinvigoration.

To examine sufficiency of 4-1BB engagement, we asked if we could replace the need for Batf3⁺ DCs in the TME at the effector phase for tumor control by directly engaging 4-1BB on the Ag-specific CD8⁺ T cells. To this end, we generated CD11c_{DTR}EGFP BM chimeras to deplete CD11c⁺ cells after both T cell priming and migration into the tumor occurred, following the experimental design depicted in Figure S1A, but then treated the mice with agonistic anti-4-1BB mAb instead of anti-PD-L1. Chimerism before tumor injection was above 90% in all groups (Figure S4E) and FTY720 efficacy was confirmed at endpoint (Figure S4F). Interestingly, the extent of tumor growth control upon agonistic anti-4-1BB treatment was similar whether in the presence or absence of CD11c⁺ DCs (Figure 4H). Accordingly, upon anti-4-1BB treatment, there was a significant increase in the number of CD8⁺SIY⁺ T cells per gram of tumor and an increase in the CD8⁺SIY⁺ T cell-to-Treg ratio, even in the absence of CD11c⁺ DCs (Figures 4I and 4J, respectively). In addition, we observed a significant decrease in the number of CD11c⁺EGFP⁺ cells and DC1s per gram of tumor upon DT

treatment, confirming DT treatment efficacy (Figures S4G and S4H, respectively). Noteworthy, contrary to the chimeras treated with anti-PD-L1, the CD11c⁺EGFP⁺ cell number and DC1 number per gram of tumor were not increased by agonistic anti-4-1BB treatment compared to the control group in the mice that were not treated with DT (Figures S1C and S1F for comparison). These results suggest that positive signals through 4-1BB engagement are critical for Ag-specific CD8⁺ T cell reinvigoration in the TME and support the notion that intratumoral Batf3⁺ DCs reinvigorate tumor-infiltrated Ag-specific CD8⁺ T cells through the 4-1BB/4-1BBL axis upon PD-L1 blockade.

It was of interest to investigate whether CD8⁺ T cell/DC1 interactions within the TME might also be associated with anti-PD-1 therapeutic efficacy in patients with cancer. Therefore, to identify DC1s by multiplex immunofluorescence (mIF), we analyzed human single-cell RNA sequencing (scRNA-seq) data from different publications^{24–27} to select a marker from the ones that have been described as being DC1-specific markers (Batf3, BDCA3, XCR1, and CLEC9A). We found that BDCA3 (THBD) was expressed on many different myeloid cells and that Batf3 and Clec9A were actually the DC1 genes to be highly expressed on DC1s (Figure S5A). However, the percentage of cells that simultaneously express CD11c and MHCII (as expected for DC1s) was higher for Batf3⁺ cells than for the rest of the DC1s markers (Figure S5B). Noteworthy, one published report characterized DC1 staining in human tumor samples and used XCR1 as a marker.²⁸ However, it was shown that at least 20% of human DC1s do not express the protein XCR1, while still expressing other known markers for DC1s, and these cells could cross-present antigens equally well to antigen-specific CD8⁺ T cells.²⁹ In addition, Poulin et al.³⁰ showed that short hairpin RNA-mediated knockdown of Batf3 selectively impairs the generation of Clec9A⁺BDCA3⁺ human DCs *in vitro*, supporting the critical role of Batf3 expression for DC1 generation not just in mice but also in human. Therefore, we chose Batf3 as the marker to identify DC1s.

We performed mIF on 41 human metastatic melanoma samples obtained at baseline, prior to anti-PD-1 treatment, and we observed CD8-staining cells and Batf3-staining cells (representative image in Figure 5A). Interestingly, we observed a correlation between the number of CD8⁺ cells and Batf3⁺ cells (Figure 5B) that was also associated with response to anti-PD-1 (Figure 5C). More specifically, when we split patients according to the median numbers of cells, we observed that cases with higher numbers of CD8⁺ cells had a significantly higher disease control rate than those with lower numbers (94.4% vs. 61.1%,

Figure 4. Positive signals delivered through 4-1BB are needed upon anti-PD-L1 treatment for Ag-specific CD8⁺ T cell accumulation and functional reinvigoration in the TME

(A) Functional analysis experimental design. One independent experiment, $n \geq 7$ per group.
(B–G) Percentage of CD8⁺SIY⁺ T cells that expressed the activation marker CD25 (B), the degranulation marker CD107a (C), and IFN- γ (D) and that are polyfunctional, IFN- γ ⁺CD107a⁺ (E), IFN- γ ⁺granzyme B⁺ (F), and IFN- γ ⁺TNF- α ⁺ (G) in the TME at day 15 after tumor injection.
(H) Tumor outgrowth of B16.SIY injected in CD11c_{DTR} BM chimeras. Same experimental design as in Figure 1A but treated with agonistic anti-4-1BB instead of anti-PD-L1, $n \geq 12$ per group.
(I) Number of CD8⁺SIY⁺ T cells per gram of tumor in each group, $n = 12$ per group.
(J) CD8⁺SIY⁺ T cell-to-Foxp3⁺ T cell ratio in each group, $n = 12$ per group.
Two independent experiments in (H)–(J). Bar graphs represent the mean values of the indicated data points, and the error bars represent SEM. ns, not significant; * $p < 0.05$, ** $p < 0.01$, *** $p < 0.001$, and **** $p < 0.0001$. Outliers were removed using GraphPad Prism with the ROUT method with a $Q = 0.1\%$. One-way ANOVA with Bonferroni's post-test (B–G, I, and J) and two-way ANOVA with Tukey's post-test (H) were used for statistical analysis.

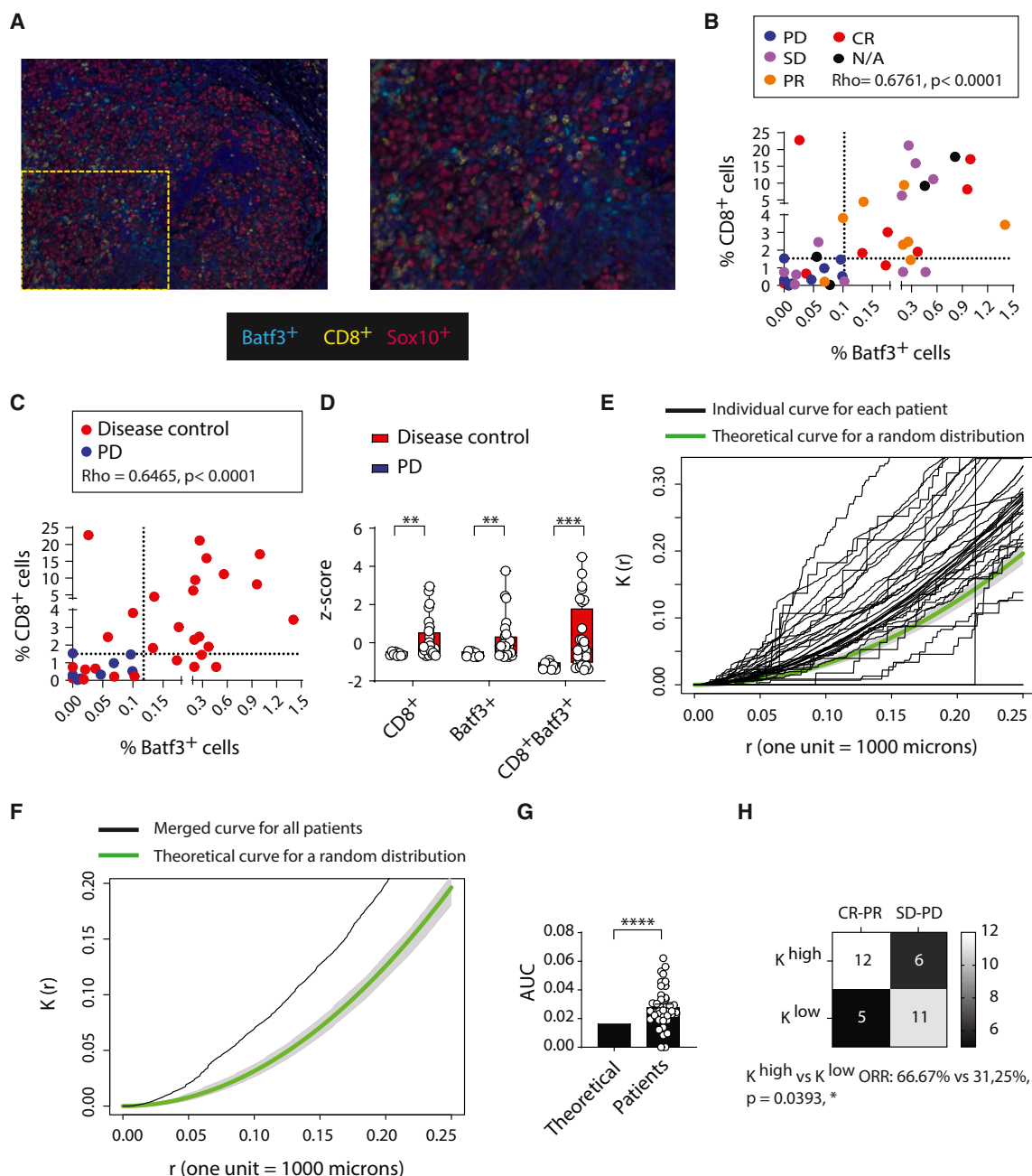


Figure 5. The number of CD8⁺ cells and Batf3⁺ cells and their clustering are associated with anti-PD-1 efficacy in human metastatic melanoma

(A) Representative image of mIF performed on human melanoma samples (left) and a zoomed region delineated with a yellow dotted rectangle (right), $n = 41$.
 (B) Correlation between the number of CD8⁺ cells and Batf3⁺ cells. Each dot represents one patient and is colored according to the clinical response to anti-PD-1 treatment. Dotted lines indicate the median for each cell type.
 (C) Correlation between the number of CD8⁺ cells and Batf3⁺ cells for the 36 patients with clinical outcome data after checkpoint blockade treatment. The disease control group includes complete response (CR), partial response (PR), and stable disease (SD).
 (D) CD8⁺ and Batf3⁺ cell Z scores for each type of cell or the sum of Z scores of both type of cells were plotted according to patient's clinical outcome.
 (E) Spatial analysis of the mIF images with the Kcross function. Each black curve represents an individual patient, and the green curve indicates the theoretical curve based on a random distribution of cells, with the confidence interval in gray, $n = 39$.
 (F) Spatial analysis where the black line represents the merged curve for all patients and the green line is the theoretical curve for a random distribution of the cells, with the confidence interval in gray.
 (G) Comparison of the patient's area under the curve (AUC) and the AUC from the theoretical curve.

(legend continued on next page)

$p = 0.0408$, Figure S5C). In addition, patients with higher numbers of Batf3⁺ cells had a significantly higher disease control rate than those with lower numbers of Batf3⁺ cells (100% vs. 55.6%, $p = 0.0029$, Figure S5D). We also integrated these parameters by normalizing the number of CD8⁺ cells and Batf3⁺ cells and calculating Z scores. Indeed, the sum of Z scores for CD8⁺ cells and Batf3⁺ cells was better at discriminating patients with disease control from patients with progressive disease compared to either parameter alone (Figure 5D). These results indicate that the number of both CD8⁺ T cells and Batf3⁺ DCs in the TME enriches for patients experiencing clinical benefit to anti-PD-1.

Upon careful analysis of the mIF images, CD8⁺ cells and Batf3⁺ cells often appeared to be in close proximity to each other. We therefore investigated whether a preferential interaction between these two cell types might be inferred and whether proximity might be predictive of anti-PD-1 efficacy. To this end, we performed an unbiased and quantitative computational spatial analysis to address if there was a favored distribution of CD8⁺ cells toward aggregation with Batf3⁺ cells. We used a modification of the Ripley's K function, which measures the number of CD8⁺ cells within a certain distance from Batf3⁺ cells, for the analysis, normalizing by CD8⁺ cell density. In Figure 5E, the individual curve for each patient is shown in black, and the theoretical curve for a random distribution of CD8⁺ cells and Batf3⁺ cells is shown in green, with its confidence interval in gray. As shown in Figure 5F, the merged curve of all patients is above the upper bound of the confidence interval of the theoretical curve for a random distribution, indicating that CD8⁺ cells are indeed preferentially clustering with Batf3⁺ cells. Accordingly, there was a significant difference between the area under the curve (AUC) of the patients and the AUC of the theoretical curve (Figure 5G). Strikingly, patients with melanoma with higher K function AUC values had a significantly higher objective response rate than patients with lower AUC values (66.7% vs. 31.25%, $p = 0.0393$; Figure 5H), demonstrating the relevance of CD8⁺ cells and Batf3⁺ clustering for PD-1 blockade efficacy. To extend these observations, we also observed a correlation between the number of CD8⁺ cells and Batf3⁺ cells (Figure S5E) and the clustering of these two types of cells (Figures S5F and S5G) in 41 muscle-invasive human bladder carcinoma primary tumor samples. Accordingly, there was also a significant difference between the AUC of the patients with bladder cancer and the AUC of the theoretical curve (Figure S5H). Taken together, our data suggest that CD8⁺ T cell-Batf3⁺ DC interactions also occur within the TME of multiple human tumor types and that such interactions are associated with anti-PD-1 efficacy.

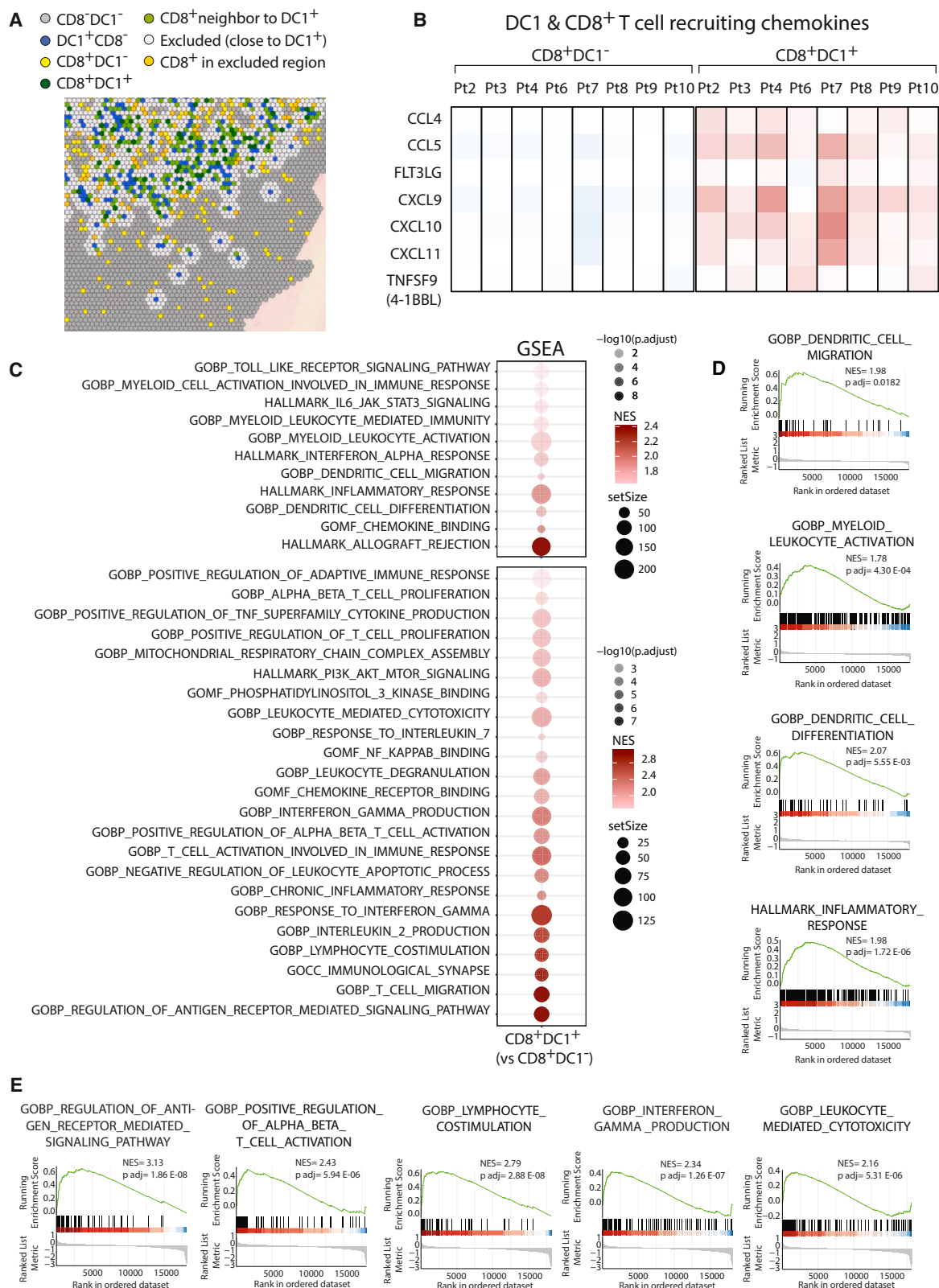
Next, to evaluate how close proximity to DC1s might be associated with CD8⁺ T cell activation state in the TME, we performed spatial transcriptomic analysis (CytAssist, Visium, 10x) on 10 human invasive carcinoma bladder samples. In all the samples, we observed spots in which DC1 genes (BATF3, CLEC9A, or XCR1

and CD11c) and CD8⁺ T cell genes (CD8A or CD8B and CD3) were co-expressed, indicating co-localization (dark green spots, Figure 6A). Accordingly, in those spots, there was a higher expression of chemokines that recruit DC1s (CCL4, CCL55, FLT3LG) and CD8⁺ T cells (CXCL9, CXCL10, CXCL11) compared to the CD8⁺ spots away from DC1s (Figure 6B).^{11,13,31} Interestingly, there was also a higher expression of TNFSF9 (4-1BBL) in the spots that expressed markers of both DC1s and CD8⁺ T cells than in the CD8⁺ spots distant from DC1⁺ spots (Figure 6B), supporting our mouse results showing the relevance of 4-1BBL expression on DC1s. As the interaction between DC1s and CD8⁺ T cells could be dynamic due to back-and-forth cell migration, we defined CD8⁺ T cells to be in close proximity to DC1s if the CD8⁺ spot was either also DC1⁺ (dark green, Figure 6A) or adjacent to a DC1⁺ spot (light green, Figure 6A). Also, as in our computational spatial analysis, we observed clustering of these cell types in the equivalent to two and a half Visium spot distances, we defined a CD8⁺ T cell spot as being distant from DC1s if the CD8⁺ spot was at least three spots away from any DC1⁺ spot (yellow spots, Figure 6A). Then, to account for variation in CD8⁺ T cell densities, we normalize gene expression to CD8 expression and compared the gene expression profile of CD8⁺DC1⁺ vs. CD8⁺DC1⁻ spots. Of note, CD8 mRNA expression has been shown to remain unchanged with T cell activation.³²

Interestingly, gene set enrichment analyses (GSEAs) showed that multiple pathways related to DC1 and T cell activation (Figure 6C, top and bottom, respectively) were significantly upregulated in CD8⁺ T cell spots in proximity to DC1s. These included pathways related to DC migration, myeloid cell activation, T cell receptor signaling, alpha-beta T cell activation, T cell co-stimulation, IFN- γ production, and leukocyte-mediated cytotoxicity (Figure 6C, and enrichment plots in Figures 6E and 6D). Prior scRNA-seq analyses had identified common gene expression patterns of CD8⁺ tumor-infiltrating lymphocytes (TILs) in different human cancer samples. These include a dysfunctional/exhausted signature,^{26,33–42} a stem-like/progenitor signature,^{26,42–46} and an activation/effector signature.^{26,33–41,43–46} We therefore sought to determine whether those transcriptional profiles that were shown to co-exist in the TME were specifically characteristic of CD8⁺ T cells adjacent to DC1s. Strikingly, we observed higher expression of genes characteristic of each of these gene signatures in CD8⁺DC1⁺ spots, including the stem-like signature state (TCF7, SLAMF6, IL-7R, BCL6, TNFRSF25, EVL; Figure 7A), the T cell activation/effector state (TNFRSF4 [OX40], TNFRSF9 [4-1BB], CD44, GZMB, PRF1, NKG7, GNLY, ITGB1, LTA [TNFB], BHLHE40, CXCL13; Figure 7B), and the dysfunctional state (HAVCR2 [Tim-3], ENTPD1 [CD39], LAG3, CTLA4, PDCD1, TIGIT, TOX, PRDM1, BATF, PAG1; Figure 7C). As these three CD8⁺ TIL differentiation states have been reported to be associated with PD-1/PD-L1 blockade clinical efficacy,^{26,27,35,36,40–42,44–46} our results link proximity of CD8⁺ TILs to DC1s in the TME with therapeutic efficacy.

(H) Heatmap representation of the number of patients with melanoma with high or low K AUC values and their clinical response to anti-PD-1 treatment. The objective response rates (ORR) in the K-high and K-low groups are indicated. Bar graphs represent the mean values of the indicated data points, and the error bars represent SEM.

* $p < 0.05$, ** $p < 0.01$, and **** $p < 0.0001$. Spearman's correlation (B and C), a two-way ANOVA with Bonferroni's post-test (D), and a one-sample t test (G) and χ^2 (H) were used for statistical analysis.



(legend on next page)

DISCUSSION

Batf3⁺ DCs have been shown to be crucial for the generation of anti-tumor immune responses, mainly because of their role in the priming of CD8⁺ T cells in the tDLNs and in the recruitment of primed effector T cells into the TME.^{9,11} Also, niches of myeloid cells/antigen-presenting cells and CD8⁺ T cells have been shown to exist in the TME and to be needed for CD8⁺ TIL maintenance and productive anti-tumor immunity.^{47–49} More recently, Meiser et al. have shown clustering of DC1s (XCR1⁺) and proliferating CD8⁺ T cells in human tumor samples.²⁸ However, whether there is a continued requirement for Batf3⁺ DCs within the TME, after the priming and recruitment phases, for the reinvigoration of dysfunctional CD8⁺ T cell upon blockade of PD-1/PD-L1 interactions had not previously been appreciated. Our data indeed indicate that intratumoral Batf3⁺ DCs are needed for the expansion/accumulation of Ag-specific CD8⁺ T cells within the TME that occurs following disruption of PD-1/PD-L1 interactions by increasing the proliferating-to-apoptotic ratio of these cells. Inasmuch as we prevented new T cell entry into the tumor before starting checkpoint blockade treatment by using FTY720, the accumulation of Ag-specific CD8⁺ T cells is unlikely to be a result of recruitment of new Ag-specific CD8⁺ T cells into the tumor site. Our results are in accordance with previous reports showing the expansion of pre-existing mouse^{20,50} and human intratumoral CD8⁺ T cells with checkpoint blockade and the importance of these cells for the therapeutic efficacy of anti-PD-1.^{4,51}

Consistent with our *in vivo* results, Duraiswamy et al.⁴⁹ showed that there are niches of CD11c⁺ cells and intraepithelial CD8⁺ T cells in tumor islets of human high-grade serous epithelial ovarian cancer and demonstrated *ex vivo* that CD11c⁺ cells are needed for anti-PD-1-mediated CD8⁺ T cell proliferation. In our current work, we determined directly *in vivo* that Batf3⁺ DCs, among the CD11c⁺ cells, are the cells needed for Ag-specific CD8⁺ T cell accumulation and checkpoint-blockade-induced tumor growth control. In addition, we detected an anti-PD-L1-induced increase in the number of DC1s in the TME that supports their relevant role in efficacy, which is in line with Barry et al.'s⁵² work, which showed a correlation between DC1 infiltration and response to anti-PD-1 in patients with melanoma. However, in our current work, with the computational spatial analysis performed on the mIF from human tumor samples, we are further showing that the number of both Batf3⁺ cells and CD8⁺ T cells and their clustering within the TME are associated with response to anti-PD-1 therapy in patients with melanoma. The close proximity between CD8⁺ T cells and Batf3⁺ DCs observed in the human TME could be explained by our spatial transcriptomics analysis showing the presence of chemokines that recruit these cells

to promote their clustering (CCL4, CCL5, and FLT3LG for DC1s and CXCL9, CXCL10, and CXCL11 for CD8⁺ TILs). These results are consistent with studies in mouse models that suggest that the CXCR3 system facilitates DC-T cell interactions within the TME^{28,31} and with our previous work showing CXCL10 production by intratumoral Batf3⁺ DCs in mouse tumors¹¹ and CD45⁺ cells in human melanoma samples.¹³ Therefore, the CXCR3/CXCL9 axis in the TME might be necessary upon PD-1 blockade treatment, not just for recruitment of activated CXCR3⁺ T cells into the TME but, additionally, for CD8⁺ TILs to come into close proximity to the DC1s and be activated through 4-1BB.

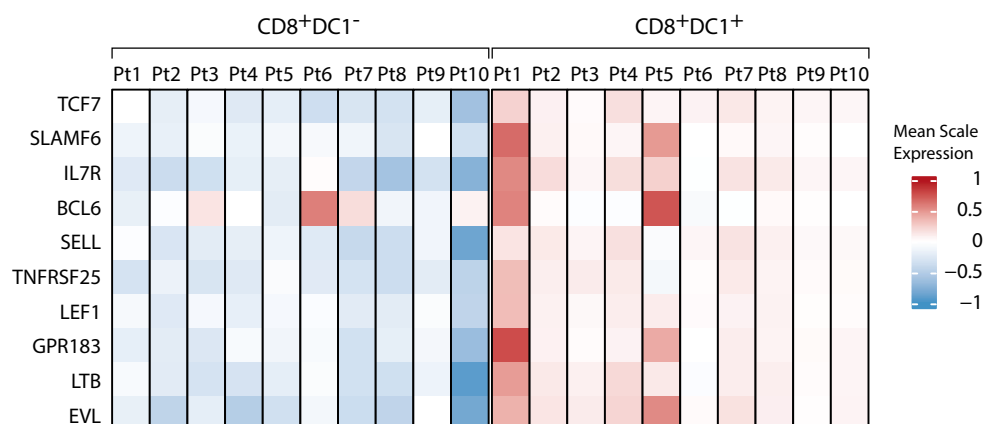
The relevance of DC1-CD8⁺ T cell interactions within the TME for PD-1 blockade efficacy could be further explained by our spatial transcriptomics GSEA, which showed enrichment of transcripts involved in adaptive immune activation in regions of the tumor with close proximity between DC1s and CD8⁺ T cells. Consistent with these results, some of the same pathways, such as T cell receptor signaling and IFN- γ , were previously found to be enriched in patients with melanoma responding to anti-PD-1.⁵³ Moreover, our spatial transcriptomics analysis of human tumor tissues indicated that DC1/CD8⁺ T cell interactions are associated with T cell acquisition of the differentiation states reported to be associated with anti-PD-1 efficacy. Our analysis also suggests that DC1s are likely involved in maintaining the stem-like CD8⁺ T cells within the tumor site and/or mediate their differentiation into the effector state, giving rise to the overall T cell-inflamed TME gene expression signature. Of note, the genes that we report here have been shown to play an active role in determining the T cell states. In addition to the known inhibitory effect of the surface markers that are part of the dysfunctional signature on CD8⁺ TILs, TOX, PRDM1, and BATF were shown to promote CD8⁺ T cell terminal differentiation/exhaustion,^{54–56} and PAG1 was demonstrated to be phosphorylated following PD-1 ligation and to mediate CD8⁺ T cell function inhibition.⁵⁷ TCF7 and BCL6 were shown to have an essential role in the generation and maintenance of the stem-like CD8⁺ T cell subset,^{58,59} while signaling through TNFRSF25 was shown to promote Ag-specific CD8⁺ TIL differentiation into cytotoxic effector cells⁶⁰ and EVL seems to be necessary for CD8⁺ T cells to form stable interactions with DCs.⁶¹ In addition to the activating role of the TNF receptor family members on CD8⁺ TILs,⁶² GZMB, PRF1, NKG7, and GNLY have been shown to be involved in CD8⁺ T cell cytotoxic activity,^{63,64} and ITGB1 (CD29) expression was shown to identify human IFN- γ -producing CD8⁺ T cells with an increased cytotoxic capability.⁶⁵ Interestingly, NKG7 and BHLHE40 expression were shown to be needed for optimal CD8⁺ TIL effector functions and for checkpoint blockade therapeutic efficacy.^{66–69} Also, the presence of

Figure 6. Strategy used for spatial transcriptomics analysis of human bladder tumor samples, heatmaps showing differential gene expression of chemokines in the CD8⁺DC1s⁺ compared to the CD8⁺DC1s[−] spots that explain co-localization of these cells, and enrichment of pathways associated with adaptive immune activation

(A) Zoomed region of representative image (shown in Figure S6) of spatial distribution of the Visium spots colored differentially according to the presence/absence of CD8⁺ T cell and DC1 gene markers.
(B) Heatmaps showing the mean-scaled gene expression of TNFSF9 (4-1BBL) and of chemokines that recruit DC1s and CD8⁺ T cells within the CD8⁺DC1⁺ and CD8⁺DC1[−] spots.
(C) GSEA showing enrichment for DC1 (top) and CD8⁺ T cell (bottom) immune activation pathways in the CD8⁺DC1⁺ spots.
(D and E) Enrichment plots for several pathways significantly enriched in the CD8⁺DC1⁺ spots related to DC1 (D) and CD8⁺ T cell (E) activation.

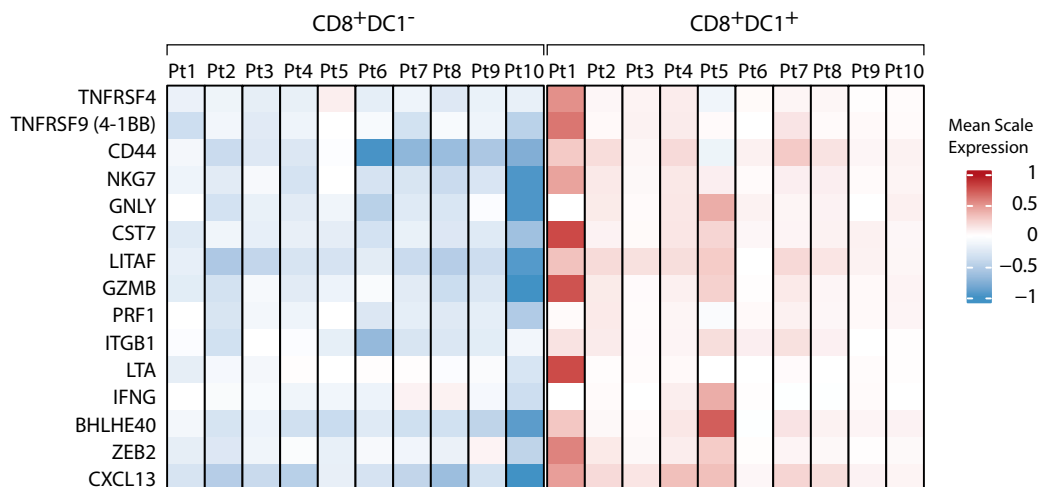
A

Stem-like CD8⁺ T cell signature



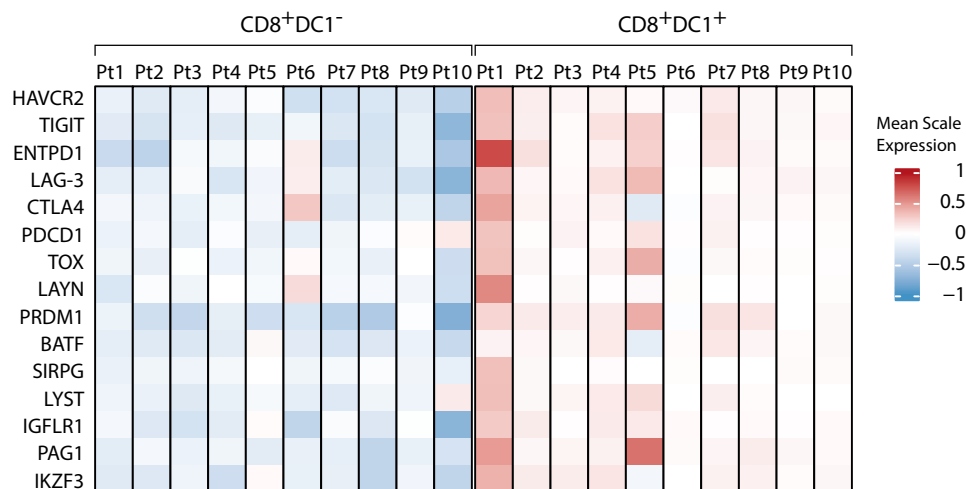
B

Activation & effector CD8⁺ T cell signature



C

Dysfunctional CD8⁺ T cell signature



(legend on next page)

CD8⁺CXCL13⁺ T cells at baseline was predictive of effective responses to PD-L1 blockade in patients with triple-negative breast cancer, and genes related to CD8⁺ T cell effector functions were upregulated in CD8⁺CXCL13⁺ T cells after treatment.²⁷ Importantly, consistent with our results, 4-1BB (TNFRSF9) was found to be highly expressed in this CD8⁺CXCL13⁺ population described by Zhang et al.,²⁷ and the expression of this marker increased after treatment.

The requirement for intratumoral Batf3⁺ DCs for local CD8⁺ T cell accumulation after PD-L1/PD-1 blockade suggests that these DCs might be providing positive co-stimulatory signals upon treatment, catalyzing T cell reinvigoration. In this regard, our current results indicate that the 4-1BB/4-1BBL axis plays a major and non-redundant role in anti-PD-L1 treatment efficacy. Indeed, we showed that DC1s express high levels of 4-1BBL and that elimination of DC1s (while other CD11c⁺ cells that express 4-1BBL were present) or blocking with anti-4-1BBL mAb prevented the anti-PD-L1-induced reinvigoration of Ag-specific CD8⁺ T cells in the TME. Moreover, we showed that administration of agonistic anti-4-1BB mAb in mice lacking DC1s could restore TIL reinvigoration and promote tumor regression. Furthermore, we showed that spatial co-localization of DC1s with CD8⁺ TILs in human tumors was associated with increased 4-1BB expression on CD8⁺ TILs and 4-1BBL expression on DC1s, correlated with anti-PD-1 efficacy and also with the T cell transcriptional profiles linked to anti-PD-1 efficacy.

4-1BB has been considered to be a marker for tumor Ag-specific activation of human CD8⁺ T cells.^{70,71} Ligation of 4-1BB has previously been shown to decrease the apoptosis and activation-induced cell death of Ag-specific CD8⁺ T cells^{72–74} and to lead to nuclear factor κ B pathway activation, which contributes to augmented T cell proliferation, cytokine production, and cytotoxicity.^{71,74–78} Enhanced mitochondrial mass and transmembrane potential in human and mouse CD8⁺ T cells, which were shown to contribute to increased T cell respiratory capacity, were also observed with 4-1BBL-mediated signaling and 4-1BB agonistic Ab treatment and in chimeric antigen receptor T cells containing 4-1BB-signaling domains.^{79–81} Our current work reveals a previously unknown role for the 4-1BB/4-1BBL axis, which is to promote and be indispensable for the accumulation and functional reinvigoration of Ag-specific CD8⁺ T cells within the TME following PD-1/PD-L1 blockade *in vivo*. Clinically, 4-1BB expression has been shown to be significantly higher in anti-PD-1-treated tumor melanoma samples than in pretreatment samples in responding patients,⁵³ and also higher in responders compared to non-responders after anti-PD-1 treatment,⁸² consistent with our results. Also, 4-1BB co-stimulation of CD8⁺ T cells was recently determined to be more potent when provided in *cis* than in *trans* with respect to CD3-T cell receptor stimulation,⁸³ which is consistent with our results showing the need for DC1s, which are dominantly cross-presenting Ag, as the most prevalent DC subset expressing 4-1BBL in the TME.

Our results have therapeutic implications, as they highlight that the presence of 4-1BBL⁺ DC1s in the TME may be rate limiting for anti-PD-1 efficacy. Thus, strategies designed to recruit and activate Batf3⁺ DCs to express the adequate ligands for CD8⁺ T cell reinvigoration in the TME might broaden checkpoint blockade efficacy. In addition, pharmacologic stimulation of 4-1BB on T cells may further improve PD-1 blockade efficacy by providing a complementary strategy in tumors with inadequate numbers of Batf3⁺ DCs or when their expression of 4-1BBL is suboptimal. While agonistic anti-4-1BB Ab treatment has been quite effective in mouse cancer models,^{84,85} clinical development has been hampered by unexpected liver toxicity.^{86,87} Still, new strategies aimed at targeting anti-4-1BB to the TME are being pursued.^{88–90} These strategies offer an attractive alternative and should enrich for engagement of 4-1BB specifically on TILs.

Limitations of the study

While this work clearly shows that DC1s are needed for anti-PD-L1 efficacy because of their role in the reinvigoration of CD8⁺ T cells in the TME upon treatment, other immune cells could affect DC1s and/or CD8⁺ T cells in the TME and therefore could also indirectly affect efficacy. Therefore, the role of other immune cells in the TME on PD-1/PD-L1 blockade efficacy deserves further study. Also, in this study, we show that the 4-1BB/4-1BBL axis is crucial for anti-PD-L1 efficacy, as removing the signaling from either side of the axis leads to a significant decrease in anti-PD-L1 efficacy, but other co-stimulatory molecules could also contribute and should be studied in the future. Our spatial transcriptomics studies provided critical data with important implications, but this technique is not at single-cell resolution and also has a shallow sequencing depth. Refined results should be enabled as the technology advances.

STAR★METHODS

Detailed methods are provided in the online version of this paper and include the following:

- KEY RESOURCES TABLE
- RESOURCE AVAILABILITY
 - Lead contact
 - Materials availability
 - Data and code availability
- EXPERIMENTAL MODEL AND STUDY PARTICIPANT DETAILS
 - Mouse strains
 - Cell lines
- METHOD DETAILS
 - Cell culture and tumor inoculation
 - Bone marrow chimeras
 - RAG2 KO experiments
 - FTY720 administration
 - Ag-specific CD8⁺ T cell functionality experiments
 - Tumor and blood processing
 - Flow cytometry
 - Immunotherapy and blocking antibodies

Figure 7. Spatial transcriptomics analysis showing that CD8⁺ TIL acquisition of the dysfunctional, stem-like, and effector gene signatures required for PD-1 blockade efficacy occurs when CD8⁺ T cells are in close proximity to DC1s in human tumor samples

Heatmaps showing scaled mean expression values of discriminative genes for the stem-like/progenitor (A), effector/activation (B), and dysfunctional/exhausted (C) CD8⁺ T cell signatures in CD8⁺DC1⁺ and CD8⁺DC1[−] spots from spatial transcriptomics analysis of 10 human bladder tumor samples.

- scRNAseq analysis for selection of the DC1 marker to be used in the multiplex immunofluorescence staining
- Multiplex Immunofluorescence staining
- Immunofluorescence spatial analysis
- Spatial transcriptomics

● QUANTIFICATION AND STATISTICAL ANALYSIS

SUPPLEMENTAL INFORMATION

Supplemental information can be found online at <https://doi.org/10.1016/j.celrep.2024.114141>.

ACKNOWLEDGMENTS

This paper is dedicated to the memory of Dr. Brendan L. Horton. The authors would like to acknowledge different cores from the University of Chicago for their assistance: the CAT Facility (RRID: SCR_017760), especially David Leclerc and Laura K. Johnston; the Animal Resource Center, especially Giovanna Christopher and Karin Kelly; and the Human Tissue Resource Center, especially Xin Jiang and Christy Schmehl. This work was enabled by infrastructure from the Human Immunologic Monitoring facility and the Functional Genomics Core of the University of Chicago Comprehensive Cancer Center. The graphical abstract was made in [BioRender.com](https://www.biorender.com). This work was supported by the NIH Outstanding Investigator Award R35 CA210098.

AUTHOR CONTRIBUTIONS

Conceptualization, T.F.G., A.Z., and B.L.H.; methodology, A.Z., B.L.H., T.F.G., and R.F.S.; investigation, A.Z., B.L.H., E.F.H., K.H., D.E.C.K., A.M., J.W.S., and Y.Z.; visualization, A.Z., E.F.H., K.H., D.E.C.K., and J.W.S.; supervision, T.F.G. and R.F.S.; writing – original draft, A.Z. and T.F.G.; writing – review & editing, all authors.

DECLARATION OF INTERESTS

T.F.G. has served on scientific advisory boards for Pyxis Oncology, Jounce Therapeutics, Allogene, MAIA, Samyang, Portal Innovations, Fog Pharma, Adaptimmune, Catalym, Bicara, and Merck; is a scientific co-founder and shareholder of Jounce Therapeutics and Pyxis Oncology; and has received research support from Bristol-Myers Squibb, Merck, Pyxis, FogPharma, and Bayer. K.H. is currently working at Merck, and D.E.C.K. is currently working at Slalom.

Received: August 30, 2023

Revised: February 29, 2024

Accepted: April 8, 2024

REFERENCES

- Topalian, S.L., Sznol, M., McDermott, D.F., Kluger, H.M., Carvajal, R.D., Sharfman, W.H., Brahmer, J.R., Lawrence, D.P., Atkins, M.B., Powderly, J.D., et al. (2014). Survival, Durable Tumor Remission, and Long-Term Safety in Patients With Advanced Melanoma Receiving Nivolumab. *J. Clin. Oncol.* 32, 1020–1030. <https://doi.org/10.1200/JCO.2013.53.0105>.
- Brahmer, J.R., Tykodi, S.S., Chow, L.Q.M., Hwu, W.-J., Topalian, S.L., Hwu, P., Drake, C.G., Camacho, L.H., Kauh, J., Odunsi, K., et al. (2012). Safety and Activity of Anti-PD-L1 Antibody in Patients with Advanced Cancer. *N. Engl. J. Med.* 366, 2455–2465. <https://doi.org/10.1056/NEJMoa1200694>.
- Larkin, J., Chiarion-Sileni, V., Gonzalez, R., Grob, J.J., Cowey, C.L., Lao, C.D., Schadendorf, D., Dummer, R., Smylie, M., Rutkowski, P., et al. (2015). Combined Nivolumab and Ipilimumab or Monotherapy in Untreated Melanoma. *N. Engl. J. Med.* 373, 23–34. <https://doi.org/10.1056/NEJMoa1504030>.
- Tumeh, P.C., Harview, C.L., Yearley, J.H., Shintaku, I.P., Taylor, E.J.M., Robert, L., Chmielowski, B., Spasic, M., Henry, G., Ciobanu, V., et al. (2014). PD-1 blockade induces responses by inhibiting adaptive immune resistance. *Nature* 515, 568–571. <https://doi.org/10.1038/nature13954>.
- Hamid, O., Robert, C., Daud, A., Hodi, F.S., Hwu, W.-J., Kefford, R., Wolchok, J.D., Hersey, P., Joseph, R.W., Weber, J.S., et al. (2013). Safety and Tumor Responses with LAMBROLIZUMAB (Anti-PD-1) in Melanoma. *N. Engl. J. Med.* 369, 134–144. <https://doi.org/10.1056/NEJMoa1305133>.
- Murphy, T.L., and Murphy, K.M. (2022). Dendritic cells in cancer immunology. *Cell. Mol. Immunol.* 19, 3–13. <https://doi.org/10.1038/s41423-021-00741-5>.
- Murphy, T.L., Grajales-Reyes, G.E., Wu, X., Tussiwand, R., Briseño, C.G., Iwata, A., Kretzer, N.M., Durai, V., and Murphy, K.M. (2016). Transcriptional Control of Dendritic Cell Development. *Annu. Rev. Immunol.* 34, 93–119. <https://doi.org/10.1146/annurev-immunol-032713-120204>.
- Edelson, B.T., KC, W., Juang, R., Kohyama, M., Benoit, L.A., Klekotka, P.A., Moon, C., Albring, J.C., Ise, W., Michael, D.G., et al. (2010). Peripheral CD103+ dendritic cells form a unified subset developmentally related to CD8 α + conventional dendritic cells. *J. Exp. Med.* 207, 823–836. <https://doi.org/10.1084/jem.20091627>.
- Fuertes, M.B., Kacha, A.K., Kline, J., Woo, S.-R., Kranz, D.M., Murphy, K.M., and Gajewski, T.F. (2011). Host type I IFN signals are required for antitumor CD8+ T cell responses through CD8 α + dendritic cells. *J. Exp. Med.* 208, 2005–2016. <https://doi.org/10.1084/jem.20101159>.
- Hildner, K., Edelson, B.T., Purtha, W.E., Diamond, M., Matsushita, H., Kohyama, M., Calderon, B., Schraml, B.U., Unanue, E.R., Diamond, M.S., et al. (2008). Batf3 Deficiency Reveals a Critical Role for CD8 α + Dendritic Cells in Cytotoxic T Cell Immunity. *Science* 322, 1097–1100. <https://doi.org/10.1126/science.1164206>.
- Spranger, S., Dai, D., Horton, B., and Gajewski, T.F. (2017). Tumor-Residing Batf3 Dendritic Cells Are Required for Effector T Cell Trafficking and Adoptive T Cell Therapy. *Cancer Cell* 31, 711–723.e4. <https://doi.org/10.1016/j.ccell.2017.04.003>.
- Spranger, S., Luke, J.J., Bao, R., Zha, Y., Hernandez, K.M., Li, Y., Gajewski, A.P., Andrade, J., and Gajewski, T.F. (2016). Density of immunogenic antigens does not explain the presence or absence of the T-cell-inflamed tumor microenvironment in melanoma. *Proc. Natl. Acad. Sci. USA* 113, E7759–E7768. <https://doi.org/10.1073/pnas.1609376113>.
- Reschke, R., Yu, J., Flood, B., Higgs, E.F., Hatogai, K., and Gajewski, T.F. (2021). Immune cell and tumor cell-derived CXCL10 is indicative of immunotherapy response in metastatic melanoma. *J. Immunother. Cancer* 9, e003521. <https://doi.org/10.1136/jitc-2021-003521>.
- Salmon, H., Idoyaga, J., Rahman, A., Leboeuf, M., Remark, R., Jordan, S., Casanova-Acebes, M., Khudoynazarova, M., Agudo, J., Tung, N., et al. (2016). Expansion and Activation of CD103+ Dendritic Cell Progenitors at the Tumor Site Enhances Tumor Responses to Therapeutic PD-L1 and BRAF Inhibition. *Immunity* 44, 924–938. <https://doi.org/10.1016/j.immuni.2016.03.012>.
- Teijera, A., Garasa, S., Luri-Rey, C., de Andrea, C., Gato, M., Molina, C., Kaisho, T., Cirella, A., Azpilikueta, A., Wculek, S.K., et al. (2022). Depletion of conventional type-1 dendritic cells in established tumors suppresses immunotherapy efficacy. *Cancer Res.* 82, 4373–4385, CAN-22-1046. <https://doi.org/10.1158/0008-5472.CAN-22-1046>.
- Moynihan, K.D., Opel, C.F., Szeto, G.L., Tzeng, A., Zhu, E.F., Engreitz, J.M., Williams, R.T., Rakhra, K., Zhang, M.H., Rothschilds, A.M., et al. (2016). Eradication of large established tumors in mice by combination immunotherapy that engages innate and adaptive immune responses. *Nat. Med.* 22, 1402–1410. <https://doi.org/10.1038/nm.4200>.
- Sánchez-Paulete, A.R., Cueto, F.J., Martínez-López, M., Labiano, S., Morales-Kastresana, A., Rodríguez-Ruiz, M.E., Jure-Kunkel, M., Azpilikueta, A., Aznar, M.A., Quetglas, J.I., et al. (2016). Cancer Immunotherapy with Immunomodulatory Anti-CD137 and Anti-PD-1 Monoclonal Antibodies Requires BATF3-Dependent Dendritic Cells. *Cancer Discov.* 6, 71–79. <https://doi.org/10.1158/2159-8290.CD-15-0510>.

18. Spiotto, M.T., Yu, P., Rowley, D.A., Nishimura, M.I., Meredith, S.C., Gajewski, T.F., Fu, Y.-X., and Schreiber, H. (2002). Increasing Tumor Antigen Expression Overcomes "Ignorance" to Solid Tumors via Crosspresentation by Bone Marrow-Derived Stromal Cells. *Immunity* 17, 737–747. [https://doi.org/10.1016/S1074-7613\(02\)00480-6](https://doi.org/10.1016/S1074-7613(02)00480-6).
19. Kline, J., Zhang, L., Battaglia, L., Cohen, K.S., and Gajewski, T.F. (2012). Cellular and Molecular Requirements for Rejection of B16 Melanoma in the Setting of Regulatory T Cell Depletion and Homeostatic Proliferation. *J. Immunol.* 188, 2630–2642. <https://doi.org/10.4049/jimmunol.1100845>.
20. Spranger, S., Koblisch, H.K., Horton, B., Scherle, P.A., Newton, R., and Gajewski, T.F. (2014). Mechanism of tumor rejection with doublets of CTLA-4, PD-1/PD-L1, or IDO blockade involves restored IL-2 production and proliferation of CD8+ T cells directly within the tumor microenvironment. *J. Immunother. Cancer* 2, 3. <https://doi.org/10.1186/2051-1426-2-3>.
21. Spranger, S., Spaapen, R.M., Zha, Y., Williams, J., Meng, Y., Ha, T.T., and Gajewski, T.F. (2013). Up-Regulation of PD-L1, IDO, and Tregs in the Melanoma Tumor Microenvironment Is Driven by CD8+ T Cells. *Sci. Transl. Med.* 5, 200ra116. <https://doi.org/10.1126/scitranslmed.3006504>.
22. Tanaka, A., and Sakaguchi, S. (2017). Regulatory T cells in cancer immunotherapy. *Cell Res.* 27, 109–118. <https://doi.org/10.1038/cr.2016.151>.
23. Principe, D.R., Chiec, L., Mohindra, N.A., and Munshi, H.G. (2021). Regulatory T-Cells as an Emerging Barrier to Immune Checkpoint Inhibition in Lung Cancer. *Front. Oncol.* 11, 684098.
24. Mulder, K., Patel, A.A., Kong, W.T., Piot, C., Halitzki, E., Dunsmore, G., Khalilnezhad, S., Irac, S.E., Dubuisson, A., Chevrier, M., et al. (2021). Cross-tissue single-cell landscape of human monocytes and macrophages in health and disease. *Immunity* 54, 1883–1900.e5. <https://doi.org/10.1016/j.immuni.2021.07.007>.
25. Steele, N.G., Carpenter, E.S., Kemp, S.B., Sirihorachai, V.R., The, S., Delrosario, L., Lazarus, J., Amir, E.A.D., Gunchick, V., Espinoza, C., et al. (2020). Multimodal mapping of the tumor and peripheral blood immune landscape in human pancreatic cancer. *Nat. Can. (Ott.)* 1, 1097–1112. <https://doi.org/10.1038/s43018-020-00121-4>.
26. Sade-Feldman, M., Yizhak, K., Bjorgaard, S.L., Ray, J.P., de Boer, C.G., Jenkins, R.W., Lieb, D.J., Chen, J.H., Frederick, D.T., Barzily-Rokni, M., et al. (2018). Defining T Cell States Associated with Response to Checkpoint Immunotherapy in Melanoma. *Cell* 175, 998–1013.e20. <https://doi.org/10.1016/j.cell.2018.10.038>.
27. Zhang, Y., Chen, H., Mo, H., Hu, X., Gao, R., Zhao, Y., Liu, B., Niu, L., Sun, X., Yu, X., et al. (2021). Single-cell analyses reveal key immune cell subsets associated with response to PD-L1 blockade in triple-negative breast cancer. *Cancer Cell* 39, 1578–1593.e8. <https://doi.org/10.1016/j.ccell.2021.09.010>.
28. Meiser, P., Knolle, M.A., Hirschberger, A., de Almeida, G.P., Bayerl, F., Lacher, S., Pedde, A.-M., Flommersfeld, S., Hönninger, J., Stark, L., et al. (2023). A distinct stimulatory cDC1 subpopulation amplifies CD8+ T cell responses in tumors for protective anti-cancer immunity. *Cancer Cell* 0. *Cancer Cell* 41, 1498–1515.e10. <https://doi.org/10.1016/j.ccell.2023.06.008>.
29. Heger, L., Hatscher, L., Liang, C., Lehmann, C.H.K., Amon, L., Lühr, J.J., Kaszubowski, T., Nziroera, R., Schaft, N., Dörrie, J., et al. (2023). XCR1 expression distinguishes human conventional dendritic cell type 1 with full effector functions from their immediate precursors. *Proc. Natl. Acad. Sci. USA* 120, e2300343120. <https://doi.org/10.1073/pnas.2300343120>.
30. Poulin, L.F., Rey, Y., Uronen-Hansson, H., Schraml, B.U., Sancho, D., Murphy, K.M., Håkansson, U.K., Moita, L.F., Agace, W.W., Bonnet, D., and Reis e Sousa, C. (2012). DNGR-1 is a specific and universal marker of mouse and human Batf3-dependent dendritic cells in lymphoid and nonlymphoid tissues. *Blood* 119, 6052–6062. <https://doi.org/10.1182/blood-2012-01-406967>.
31. Chow, M.T., Ozga, A.J., Servis, R.L., Frederick, D.T., Lo, J.A., Fisher, D.E., Freeman, G.J., Boland, G.M., and Luster, A.D. (2019). Intratumoral Activity of the CXCR3 Chemokine System Is Required for the Efficacy of Anti-PD-1 Therapy. *Immunity* 50, 1498–1512.e5. <https://doi.org/10.1016/j.immuni.2019.04.010>.
32. Xiao, Z., Mescher, M.F., and Jameson, S.C. (2007). Detuning CD8 T cells: down-regulation of CD8 expression, tetramer binding, and response during CTL activation. *J. Exp. Med.* 204, 2667–2677. <https://doi.org/10.1084/jem.20062376>.
33. Guo, X., Zhang, Y., Zheng, L., Zheng, C., Song, J., Zhang, Q., Kang, B., Liu, Z., Jin, L., Xing, R., et al. (2018). Global characterization of T cells in non-small-cell lung cancer by single-cell sequencing. *Nat. Med.* 24, 978–985. <https://doi.org/10.1038/s41591-018-0045-3>.
34. Li, H., van der Leun, A.M., Yofe, I., Lubling, Y., Gelbard-Solodkin, D., van Akkooi, A.C.J., van den Braber, M., Rozeman, E.A., Haanen, J.B.A.G., Blank, C.U., et al. (2019). Dysfunctional CD8 T Cells Form a Proliferative, Dynamically Regulated Compartment within Human Melanoma. *Cell* 176, 775–789.e18. <https://doi.org/10.1016/j.cell.2018.11.043>.
35. Siddiqui, I., Schaeuble, K., Chennupati, V., Fuertes Marraco, S.A., Calderon-Copete, S., Pais Ferreira, D., Carmona, S.J., Scarpellino, L., Gfeller, D., Pradervand, S., et al. (2019). Intratumoral Tcf1+PD-1+CD8+ T Cells with Stem-like Properties Promote Tumor Control in Response to Vaccination and Checkpoint Blockade Immunotherapy. *Immunity* 50, 195–211.e10. <https://doi.org/10.1016/j.immuni.2018.12.021>.
36. Thommen, D.S., Koelzer, V.H., Herzig, P., Roller, A., Trefny, M., Dimeloe, S., Kiialainen, A., Hanhart, J., Schill, C., Hess, C., et al. (2018). A transcriptionally and functionally distinct PD-1+ CD8+ T cell pool with predictive potential in non-small-cell lung cancer treated with PD-1 blockade. *Nat. Med.* 24, 994–1004. <https://doi.org/10.1038/s41591-018-0057-z>.
37. Tirosh, I., Izar, B., Prakadan, S.M., Wadsworth, M.H., Treacy, D., Trombetta, J.J., Rotem, A., Rodman, C., Lian, C., Murphy, G., et al. (2016). Dissecting the multicellular ecosystem of metastatic melanoma by single-cell RNA-seq. *Science* 352, 189–196. <https://doi.org/10.1126/science.aad0501>.
38. Zheng, C., Zheng, L., Yoo, J.-K., Guo, H., Zhang, Y., Guo, X., Kang, B., Hu, R., Huang, J.Y., Zhang, Q., et al. (2017). Landscape of Infiltrating T Cells in Liver Cancer Revealed by Single-Cell Sequencing. *Cell* 169, 1342–1356.e16. <https://doi.org/10.1016/j.cell.2017.05.035>.
39. Zhang, L., Yu, X., Zheng, L., Zhang, Y., Li, Y., Fang, Q., Gao, R., Kang, B., Zhang, Q., Huang, J.Y., et al. (2018). Lineage tracking reveals dynamic relationships of T cells in colorectal cancer. *Nature* 564, 268–272. <https://doi.org/10.1038/s41586-018-0694-x>.
40. Liu, B., Hu, X., Feng, K., Gao, R., Xue, Z., Zhang, S., Zhang, Y., Corse, E., Hu, Y., Han, W., and Zhang, Z. (2022). Temporal single-cell tracing reveals clonal revival and expansion of precursor exhausted T cells during anti-PD-1 therapy in lung cancer. *Nat. Can. (Ott.)* 3, 108–121. <https://doi.org/10.1038/s43018-021-00292-8>.
41. Bassez, A., Vos, H., Van Dyck, L., Floris, G., Arijis, I., Desmedt, C., Boeckx, B., Vanden Bempt, M., Nevelsteen, I., Lambein, K., et al. (2021). A single-cell map of intratumoral changes during anti-PD1 treatment of patients with breast cancer. *Nat. Med.* 27, 820–832. <https://doi.org/10.1038/s41591-021-01323-8>.
42. Zehn, D., Thimme, R., Lugli, E., de Almeida, G.P., and Oxenius, A. (2022). 'Stem-like' precursors are the fount to sustain persistent CD8+ T cell responses. *Nat. Immunol.* 23, 836–847. <https://doi.org/10.1038/s41590-022-01219-w>.
43. Brummelman, J., Mazza, E.M.C., Alvisi, G., Colombo, F.S., Grilli, A., Mikulak, J., Mavilio, D., Alloisio, M., Ferrari, F., Lopci, E., et al. (2018). High-dimensional single cell analysis identifies stem-like cytotoxic CD8+ T cells infiltrating human tumors. *J. Exp. Med.* 215, 2520–2535. <https://doi.org/10.1084/jem.20180684>.
44. Kurtulus, S., Madi, A., Escobar, G., Klapholz, M., Nyman, J., Christian, E., Pawlak, M., Dionne, D., Xia, J., Rozenblatt-Rosen, O., et al. (2019). Checkpoint Blockade Immunotherapy Induces Dynamic Changes in PD-1-CD8+ Tumor-Infiltrating T Cells. *Immunity* 50, 181–194.e6. <https://doi.org/10.1016/j.immuni.2018.11.014>.

45. Caushi, J.X., Zhang, J., Ji, Z., Vaghiasa, A., Zhang, B., Hsiue, E.H.-C., Mog, B.J., Hou, W., Justesen, S., Blosser, R., et al. (2021). Transcriptional programs of neoantigen-specific TIL in anti-PD-1-treated lung cancers. *Nature* 596, 126–132. <https://doi.org/10.1038/s41586-021-03752-4>.
46. Miller, B.C., Sen, D.R., Al Abosy, R., Bi, K., Virkud, Y.V., LaFleur, M.W., Yates, K.B., Lako, A., Felt, K., Naik, G.S., et al. (2019). Subsets of exhausted CD8⁺ T cells differentially mediate tumor control and respond to checkpoint blockade. *Nat. Immunol.* 20, 326–336. <https://doi.org/10.1038/s41590-019-0312-6>.
47. Jansen, C.S., Prokhnevskaya, N., Master, V.A., Sanda, M.G., Carlisle, J.W., Bilen, M.A., Cardenas, M., Wilkinson, S., Lake, R., Sowalsky, A.G., et al. (2019). An intra-tumoral niche maintains and differentiates stem-like CD8 T cells. *Nature* 576, 465–470. <https://doi.org/10.1038/s41586-019-1836-5>.
48. Prokhnevskaya, N., Cardenas, M.A., Valanparambil, R.M., Sobierajska, E., Barwick, B.G., Jansen, C., Reyes Moon, A., Gregorova, P., delBalzo, L., Greenwald, R., et al. (2023). CD8⁺ T cell activation in cancer comprises an initial activation phase in lymph nodes followed by effector differentiation within the tumor. *Immunity* 56, 107–124.e5. <https://doi.org/10.1016/j.immuni.2022.12.002>.
49. Duraiswamy, J., Turrini, R., Minasyan, A., Barras, D., Crespo, I., Grimm, A.J., Casado, J., Genolet, R., Benedetti, F., Wicky, A., et al. (2021). Myeloid antigen-presenting cell niches sustain antitumor T cells and license PD-1 blockade via CD28 costimulation. *Cancer Cell* 39, 1623–1642.e20. <https://doi.org/10.1016/j.ccell.2021.10.008>.
50. Garris, C.S., Arlauckas, S.P., Kohler, R.H., Trefny, M.P., Garren, S., Piot, C., Engblom, C., Pfirschke, C., Siwicki, M., Gungabeesoon, J., et al. (2018). Successful Anti-PD-1 Cancer Immunotherapy Requires T Cell-Dendritic Cell Crosstalk Involving the Cytokines IFN- γ and IL-12. *Immunity* 49, 1148–1161.e7. <https://doi.org/10.1016/j.immuni.2018.09.024>.
51. Voabil, P., de Bruijn, M., Roelofs, L.M., Hendriks, S.H., Brokamp, S., van den Braber, M., Broeks, A., Sanders, J., Herzog, P., Zippelius, A., et al. (2021). An ex vivo tumor fragment platform to dissect response to PD-1 blockade in cancer. *Nat. Med.* 27, 1250–1261. <https://doi.org/10.1038/s41591-021-01398-3>.
52. Barry, K.C., Hsu, J., Broz, M.L., Cueto, F.J., Binnewies, M., Combes, A.J., Nelson, A.E., Loo, K., Kumar, R., Rosenblum, M.D., et al. (2018). A natural killer–dendritic cell axis defines checkpoint therapy–responsive tumor microenvironments. *Nat. Med.* 24, 1178–1191. <https://doi.org/10.1038/s41591-018-0085-8>.
53. Riaz, N., Havel, J.J., Makarov, V., Desrichard, A., Urba, W.J., Sims, J.S., Hodi, F.S., Martín-Algarra, S., Mandal, R., Sharfman, W.H., et al. (2017). Tumor and Microenvironment Evolution during Immunotherapy with Nivolumab. *Cell* 171, 934–949.e16. <https://doi.org/10.1016/j.cell.2017.09.028>.
54. Scott, A.C., Dündar, F., Zumbo, P., Chandran, S.S., Klebanoff, C.A., Shakiba, M., Trivedi, P., Menocal, L., Appleby, H., Camara, S., et al. (2019). TOX is a critical regulator of tumour-specific T cell differentiation. *Nature* 571, 270–274. <https://doi.org/10.1038/s41586-019-1324-y>.
55. Shin, H., Blackburn, S.D., Intlekofer, A.M., Kao, C., Angelosanto, J.M., Reiner, S.L., and Wherry, E.J. (2009). A Role for the Transcriptional Repressor Blimp-1 in CD8⁺ T Cell Exhaustion during Chronic Viral Infection. *Immunity* 31, 309–320. <https://doi.org/10.1016/j.immuni.2009.06.019>.
56. Quigley, M., Pereyra, F., Nilsson, B., Porichis, F., Fonseca, C., Eichbaum, Q., Julg, B., Jesneck, J.L., Brosnahan, K., Imam, S., et al. (2010). Transcriptional analysis of HIV-specific CD8⁺ T cells shows that PD-1 inhibits T cell function by upregulating BATF. *Nat. Med.* 16, 1147–1151. <https://doi.org/10.1038/nm.2232>.
57. Strazza, M., Azoulay-Alfaguter, I., Peled, M., Adam, K., and Mor, A. (2021). Transmembrane adaptor protein PAG is a mediator of PD-1 inhibitory signaling in human T cells. *Commun. Biol.* 4, 672. <https://doi.org/10.1038/s42003-021-02225-8>.
58. Wu, T., Ji, Y., Moseman, E.A., Xu, H.C., Mangani, M., Kirby, M., Anderson, S.M., Handon, R., Kenyon, E., Elkahlon, A., et al. (2016). The TCF1-Bcl6 axis counteracts type I interferon to repress exhaustion and maintain T cell stemness. *Sci. Immunol.* 1, eaai8593. <https://doi.org/10.1126/sciimmunol.aai8593>.
59. Im, S.J., Hashimoto, M., Gerner, M.Y., Lee, J., Kissick, H.T., Burger, M.C., Shan, Q., Hale, J.S., Lee, J., Nasti, T.H., et al. (2016). Defining CD8⁺ T cells that provide the proliferative burst after PD-1 therapy. *Nature* 537, 417–421. <https://doi.org/10.1038/nature19330>.
60. Slebiada, T.J., Rowley, T.F., Ferdinand, J.R., Willoughby, J.E., Buchan, S.L., Taraban, V.Y., and Al-Shamkhani, A. (2011). Triggering of TNFRSF25 promotes CD8⁺ T-cell responses and anti-tumor immunity. *Eur. J. Immunol.* 41, 2606–2611. <https://doi.org/10.1002/eji.201141477>.
61. Waldman, M.M., Rahkola, J.T., Sigler, A.L., Chung, J.W., Willett, B.A.S., Kedl, R.M., Friedman, R.S., and Jacobelli, J. (2022). Ena/VASP Protein-Mediated Actin Polymerization Contributes to Naïve CD8⁺ T Cell Activation and Expansion by Promoting T Cell-APC Interactions In Vivo. *Front. Immunol.* 13, 856977. <https://doi.org/10.3389/fimmu.2022.856977>.
62. Croft, M. (2009). The role of TNF superfamily members in T-cell function and diseases. *Nat. Rev. Immunol.* 9, 271–285. <https://doi.org/10.1038/nri2526>.
63. Ng, S.S., De Labastida Rivera, F., Yan, J., Corvino, D., Das, I., Zhang, P., Kuns, R., Chauhan, S.B., Hou, J., Li, X.-Y., et al. (2020). The NK cell granule protein NKG7 regulates cytotoxic granule exocytosis and inflammation. *Nat. Immunol.* 21, 1205–1218. <https://doi.org/10.1038/s41590-020-0758-6>.
64. Peña, S.V., Hanson, D.A., Carr, B.A., Goralski, T.J., and Krensky, A.M. (1997). Processing, subcellular localization, and function of 519 (granulysin), a human late T cell activation molecule with homology to small, lytic, granule proteins. *J. Immunol.* 158, 2680–2688. <https://doi.org/10.4049/jimmunol.158.6.2680>.
65. Nicolet, B.P., Guislain, A., van Alphen, F.P.J., Gomez-Eerland, R., Schumacher, T.N.M., van den Biggelaar, M., and Wolkers, M.C. (2020). CD29 identifies IFN- γ -producing human CD8⁺ T cells with an increased cytotoxic potential. *Proc. Natl. Acad. Sci. USA* 117, 6686–6696. <https://doi.org/10.1073/pnas.1913940117>.
66. Li, X.-Y., Corvino, D., Nowlan, B., Aguilera, A.R., Ng, S.S., Braun, M., Cillo, A.R., Bald, T., Smyth, M.J., and Engwerda, C.R. (2022). NKG7 Is Required for Optimal Antitumor T-cell Immunity. *Cancer Immunol. Res.* 10, 154–161. <https://doi.org/10.1158/2326-6066.CIR-20-0649>.
67. Wen, T., Barham, W., Li, Y., Zhang, H., Gicobi, J.K., Hirdler, J.B., Liu, X., Ham, H., Peterson Martinez, K.E., Lucien, F., et al. (2022). NKG7 Is a T-cell-Intrinsic Therapeutic Target for Improving Antitumor Cytotoxicity and Cancer Immunotherapy. *Cancer Immunol. Res.* 10, 162–181. <https://doi.org/10.1158/2326-6066.CIR-21-0539>.
68. Li, C., Zhu, B., Son, Y.M., Wang, Z., Jiang, L., Xiang, M., Ye, Z., Beckermann, K.E., Wu, Y., Jenkins, J.W., et al. (2019). The Transcription Factor Bhlhe40 Programs Mitochondrial Regulation of Resident CD8⁺ T Cell Fitness and Functionality. *Immunity* 51, 491–507.e7. <https://doi.org/10.1016/j.immuni.2019.08.013>.
69. Salmon, A.J., Shavkunov, A.S., Miao, Q., Jarjour, N.N., Keshari, S., Esaulova, E., Williams, C.D., Ward, J.P., Highsmith, A.M., Pineda, J.E., et al. (2022). BHLHE40 Regulates the T-Cell Effector Function Required for Tumor Microenvironment Remodeling and Immune Checkpoint Therapy Efficacy. *Cancer Immunol. Res.* 10, 597–611. <https://doi.org/10.1158/2326-6066.CIR-21-0129>.
70. Wolff, M., Kuball, J., Ho, W.Y., Nguyen, H., Manley, T.J., Bleakley, M., and Greenberg, P.D. (2007). Activation-induced expression of CD137 permits detection, isolation, and expansion of the full repertoire of CD8⁺ T cells responding to antigen without requiring knowledge of epitope specificities. *Blood* 110, 201–210. <https://doi.org/10.1182/blood-2006-11-056168>.
71. Ye, Q., Song, D.-G., Poussin, M., Yamamoto, T., Best, A., Li, C., Coukos, G., and Powell, D.J. (2014). CD137 Accurately Identifies and Enriches for Naturally Occurring Tumor-Reactive T Cells in Tumor. *Clin. Cancer Res.* 20, 44–55. <https://doi.org/10.1158/1078-0432.CCR-13-0945>.

72. Sabbagh, L., Pulle, G., Liu, Y., Tsitsikov, E.N., and Watts, T.H. (2008). ERK-Dependent Bim Modulation Downstream of the 4-1BB-TRAF1 Signaling Axis Is a Critical Mediator of CD8 T Cell Survival In Vivo. *J. Immunol.* 180, 8093–8101. <https://doi.org/10.4049/jimmunol.180.12.8093>.
73. Horton, B.L., Williams, J.B., Cabanov, A., Spranger, S., and Gajewski, T.F. (2018). Intratumoral CD8+ T-cell Apoptosis Is a Major Component of T-cell Dysfunction and Impedes Antitumor Immunity. *Cancer Immunol. Res.* 6, 14–24. <https://doi.org/10.1158/2326-6066.CIR-17-0249>.
74. Hernandez-Chacon, J.A., Li, Y., Wu, R.C., Bernatchez, C., Wang, Y., Weber, J.S., Hwu, P., and Radvanyi, L.G. (2011). Costimulation Through the CD137/4-1BB Pathway Protects Human Melanoma Tumor-Infiltrating Lymphocytes From Activation-induced Cell Death and Enhances Antitumor Effector Function. *J. Immunother.* 34, 236–250. <https://doi.org/10.1097/CJI.0b013e318209e7ec>.
75. Lee, H.-W., Nam, K.-O., Park, S.-J., and Kwon, B.S. (2003). 4-1BB enhances CD8+ T cell expansion by regulating cell cycle progression through changes in expression of cyclins D and E and cyclin-dependent kinase inhibitor p27kip1. *Eur. J. Immunol.* 33, 2133–2141. <https://doi.org/10.1002/eji.200323996>.
76. Wen, T., Bukczynski, J., and Watts, T.H. (2002). 4-1BB ligand-mediated costimulation of human T cells induces CD4 and CD8 T cell expansion, cytokine production, and the development of cytolytic effector function. *J. Immunol.* 168, 4897–4906. <https://doi.org/10.4049/jimmunol.168.10.4897>.
77. Shuford, W.W., Klussman, K., Tritchler, D.D., Loo, D.T., Chalupny, J., Siadak, A.W., Brown, T.J., Emswiler, J., Raecho, H., Larsen, C.P., et al. (1997). 4-1BB Costimulatory Signals Preferentially Induce CD8+ T Cell Proliferation and Lead to the Amplification In Vivo of Cytotoxic T Cell Responses. *J. Exp. Med.* 186, 47–55. <https://doi.org/10.1084/jem.186.1.47>.
78. Laderach, D., Movassagh, M., Johnson, A., Mittler, R.S., and Galy, A. (2002). 4-1BB co-stimulation enhances human CD8+ T cell priming by augmenting the proliferation and survival of effector CD8+ T cells. *Int. Immunol.* 14, 1155–1167. <https://doi.org/10.1093/intimm/14.10.1155>.
79. Teixeira, A., Labiano, S., Garasa, S., Etxeberria, I., Santamaría, E., Rouzaut, A., Enamorado, M., Azpilikueta, A., Inoges, S., Bolaños, E., et al. (2018). Mitochondrial Morphological and Functional Reprogramming Following CD137 (4-1BB) Costimulation. *Cancer Immunol. Res.* 6, 798–811. <https://doi.org/10.1158/2326-6066.CIR-17-0767>.
80. Menk, A.V., Scharping, N.E., Rivadeneira, D.B., Calderon, M.J., Watson, M.J., Dunstane, D., Watkins, S.C., and Delgoffe, G.M. (2018). 4-1BB costimulation induces T cell mitochondrial function and biogenesis enabling cancer immunotherapeutic responses. *J. Exp. Med.* 215, 1091–1100. <https://doi.org/10.1084/jem.20171068>.
81. Kawalekar, O.U., O'Connor, R.S., Fraietta, J.A., Guo, L., McGettigan, S.E., Posey, A.D., Patel, P.R., Guedan, S., Scholler, J., Keith, B., et al. (2016). Distinct Signaling of Coreceptors Regulates Specific Metabolism Pathways and Impacts Memory Development in CAR T Cells. *Immunity* 44, 380–390. <https://doi.org/10.1016/j.immuni.2016.01.021>.
82. Chen, P.-L., Roh, W., Reuben, A., Cooper, Z.A., Spencer, C.N., Prieto, P.A., Miller, J.P., Bassett, R.L., Gopalakrishnan, V., Wani, K., et al. (2016). Analysis of Immune Signatures in Longitudinal Tumor Samples Yields Insight into Biomarkers of Response and Mechanisms of Resistance to Immune Checkpoint Blockade. *Cancer Discov.* 6, 827–837. <https://doi.org/10.1158/2159-8290.CD-15-1545>.
83. Otano, I., Azpilikueta, A., Glez-Vaz, J., Alvarez, M., Medina-Echeverez, J., Cortés-Domínguez, I., Ortiz-de-Solorzano, C., Ellmark, P., Fritzell, S., Hernandez-Hoyos, G., et al. (2021). CD137 (4-1BB) costimulation of CD8+ T cells is more potent when provided in cis than in trans with respect to CD3-TCR stimulation. *Nat. Commun.* 12, 7296. <https://doi.org/10.1038/s41467-021-27613-w>.
84. Melero, I., Shuford, W.W., Newby, S.A., Aruffo, A., Ledbetter, J.A., Hellström, K.E., Mittler, R.S., and Chen, L. (1997). Monoclonal antibodies against the 4-1BB T-cell activation molecule eradicate established tumors. *Nat. Med.* 3, 682–685. <https://doi.org/10.1038/nm0697-682>.
85. Etxeberria, I., Glez-Vaz, J., Teixeira, Á., and Melero, I. (2020). New emerging targets in cancer immunotherapy: CD137/4-1BB costimulatory axis. *ESMO Open* 4, e000733. <https://doi.org/10.1136/esmoopen-2020-000733>.
86. Segal, N.H., Logan, T.F., Hodi, F.S., McDermott, D., Melero, I., Hamid, O., Schmidt, H., Robert, C., Chiarion-Sileni, V., Ascierto, P.A., et al. (2017). Results from an Integrated Safety Analysis of Urelumab, an Agonist Anti-CD137 Monoclonal Antibody. *Clin. Cancer Res.* 23, 1929–1936. <https://doi.org/10.1158/1078-0432.CCR-16-1272>.
87. Segal, N.H., He, A.R., Doi, T., Levy, R., Bhatia, S., Pishvaian, M.J., Cesari, R., Chen, Y., Davis, C.B., Huang, B., et al. (2018). Phase I Study of Single-Agent Utomilumab (PF-05082566), a 4-1BB/CD137 Agonist, in Patients with Advanced Cancer. *Clin. Cancer Res.* 24, 1816–1823. <https://doi.org/10.1158/1078-0432.CCR-17-1922>.
88. Kamata-Sakurai, M., Narita, Y., Hori, Y., Nemoto, T., Uchikawa, R., Honda, M., Hironiwa, N., Taniguchi, K., Shida-Kawazoe, M., Metsugi, S., et al. (2021). Antibody to CD137 Activated by Extracellular Adenosine Triphosphate Is Tumor Selective and Broadly Effective In Vivo without Systemic Immune Activation. *Cancer Discov.* 11, 158–175. <https://doi.org/10.1158/2159-8290.CD-20-0328>.
89. Hurov, K., Lahdenranta, J., Upadhyaya, P., Haines, E., Cohen, H., Repash, E., Kanakia, D., Ma, J., Kristensson, J., You, F., et al. (2021). BT7480, a novel fully synthetic Bicycle tumor-targeted immune cell agonistTM (Bicycle TICATM) induces tumor localized CD137 agonism. *J. Immunother. Cancer* 9, e002883. <https://doi.org/10.1136/jitc-2021-002883>.
90. Claus, C., Ferrara, C., Xu, W., Sam, J., Lang, S., Uhlenbrock, F., Albrecht, R., Herter, S., Schlenker, R., Hüscher, T., et al. (2019). Tumor-targeted 4-1BB agonists for combination with T cell bispecific antibodies as off-the-shelf therapy. *Sci. Transl. Med.* 11, eaav5989. <https://doi.org/10.1126/scitranslmed.aav5989>.
91. Hao, Y., Hao, S., Andersen-Nissen, E., Mauck, W.M., Zheng, S., Butler, A., Lee, M.J., Wilk, A.J., Darby, C., Zager, M., et al. (2021). Integrated analysis of multimodal single-cell data. *Cell* 184, 3573–3587.e29. <https://doi.org/10.1016/j.cell.2021.04.048>.
92. Dries, R., Zhu, Q., Dong, R., Eng, C.-H.L., Li, H., Liu, K., Fu, Y., Zhao, T., Sarkar, A., Bao, F., et al. (2021). Giotto: a toolbox for integrative analysis and visualization of spatial expression data. *Genome Biol.* 22, 78. <https://doi.org/10.1186/s13059-021-02286-2>.
93. Subramanian, A., Tamayo, P., Mootha, V.K., Mukherjee, S., Ebert, B.L., Gillette, M.A., Paulovich, A., Pomeroy, S.L., Golub, T.R., Lander, E.S., and Mesirov, J.P. (2005). Gene set enrichment analysis: A knowledge-based approach for interpreting genome-wide expression profiles. *Proc. Natl. Acad. Sci. USA* 102, 15545–15550. <https://doi.org/10.1073/pnas.0506580102>.
94. Yu, G., Wang, L.-G., Han, Y., and He, Q.-Y. (2012). clusterProfiler: an R package for comparing biological themes among gene clusters. *OMICS* 16, 284–287. <https://doi.org/10.1089/omi.2011.0118>.
95. Gu, Z., Eils, R., and Schlesner, M. (2016). Complex heatmaps reveal patterns and correlations in multidimensional genomic data. *Bioinformatics* 32, 2847–2849. <https://doi.org/10.1093/bioinformatics/btw313>.

STAR★METHODS

KEY RESOURCES TABLE

REAGENT or RESOURCE	SOURCE	IDENTIFIER
Antibodies		
Ki67 BV711	BD Bioscience	RRID: AB_2738406
Ki67 BUV395	BD Bioscience	RRID: AB_2738577
Active Caspase-3 BV605	BD Bioscience	RRID: AB_2738589
Active Caspase-3 AF647	BD Bioscience	RRID: AB_1727414
CD4 BV480	BD Bioscience	RRID: AB_2743777
CD317 BV480	BD Bioscience	RRID: AB_2744168
CD8a FITC	BD Bioscience	RRID: AB_394569
CD8a BUV395	BD Bioscience	RRID: AB_2739421
CD4 BUV805	BD Bioscience	RRID: AB_2739008
CD45.1 BUV496	BD Bioscience	RRID: AB_2870692
CD11c BUV395	BD Bioscience	RRID: AB_2738580
CD317 BUV805	BD Bioscience	RRID: AB_2873648
NK1.1 BV650	BD Bioscience	RRID: AB_2738617
Ly6G BUV661	BD Bioscience	RRID: AB_2871000
CD3 BUV496	BD Bioscience	RRID: AB_2870231
CD3 BUV563	BD Bioscience	RRID: AB_2870837
CD4 BUV563	BD Bioscience	RRID: AB_2870208
NK1.1 BV480	BD Bioscience	RRID: AB_2743597
CD279 APC-R700	BD Bioscience	RRID: AB_2739366
CD223 BUV496	BD Bioscience	RRID: AB_2874245
CD107a BV786	BD Bioscience	RRID: AB_2738762
CD25 BB515	BD Bioscience	RRID: AB_2738803
IFN- γ BUV737	BD Bioscience	RRID: AB_2870098
CD8a Pacific Blue	Biolegend	RRID: AB_493426
CD45.1 APC-Cy7	Biolegend	RRID: AB_313504
CD45.2 BV785	Biolegend	RRID: AB_2562604
CD3 AF700	Biolegend	RRID: AB_493696
CD279 BV510	Biolegend	RRID: AB_2715761
CD19 BV510	Biolegend	RRID: AB_2562137
CD103 BV711	Biolegend	RRID: AB_2686970
I-A/I-E Pacific Blue	Biolegend	RRID: AB_493527
CD11b BV750	Biolegend	RRID: AB_2810328
CD45.2 APC-Cy7	Biolegend	RRID: AB_830788
CD8a BV605	Biolegend	RRID: AB_2561352
CD11c AF647	Biolegend	RRID: AB_389328
NK1.1 BV421	Biolegend	RRID: AB_2562218
NK1.1 APC/Fire810	Biolegend	RRID: AB_2894654
CD45 BV510	Biolegend	RRID: AB_2561392
CD45 Pacific Blue	Biolegend	RRID: AB_493536
CD3 PE	Biolegend	RRID: AB_312673
CD4 BV711	Biolegend	RRID: AB_11219396
CD279 PE-Cy7	Biolegend	RRID: AB_572016
CD223 APC	Biolegend	RRID: AB_10639935
CD137 APC	Biolegend	RRID: AB_2564296

(Continued on next page)

Continued

REAGENT or RESOURCE	SOURCE	IDENTIFIER
CD11b AF700	Biolegend	RRID: AB_493705
I-A/I-E APC-Fire750	Biolegend	RRID: AB_2616728
Ly6C Pacific Blue	Biolegend	RRID: AB_1732079
CD19 PerCP-Cy5.5	Biolegend	RRID: AB_2072925
CD103 BV785	Biolegend	RRID: AB_2800588
Ki67 BV421	Biolegend	RRID: AB_2562663
TNF-alpha AF647	Biolegend	RRID: AB_493330
IL-2 PE/Cy5	Biolegend	RRID: AB_2123674
Granzyme B PE/Cy7	Biolegend	RRID: AB_2728380
CD3 PerCP/Cy5.5	Biolegend	RRID: AB_2629844
Zombie NIR Fixable Viability Kit	Biolegend	Cat# 423106
Purified anti-mouse CD16/32 Antibody (Fc block)	Biolegend	RRID:AB_312801
CD223 PerCPeFluo	eBioscience	RRID: AB_11151334
Foxp3 APC	eBioscience	RRID: AB_469456
CD45.1 PerCP-Cy5.5	eBioscience	RRID: AB_1107003
CD137 eFluor450	eBioscience	RRID: AB_2574041
NK1.1 PerCP/Cy5.5	eBioscience	RRID: AB_914361
CD137 PE-Cy7	eBioscience	RRID: AB_2573398
CD45.2 AF532	eBioscience	RRID: AB_2815270
CD45 AF532	eBioscience	RRID: AB_11218871
F4/80 PE-Cy5	eBioscience	RRID: AB_468798
CD137L (41BBL) Biotin	eBioscience	RRID: AB_466788
CD8 APC-eF780	eBioscience	RRID: AB_1272185
Foxp3 eFluor506	eBioscience	RRID: AB_2637367
Fixable viability dye eFluor 780	eBioscience	Cat# 65-0865-18
Fixable viability dye eFluor 506	eBioscience	Cat# 65-0866-18
InVivoPlus anti-mouse PD-L1 (B7-H1)	Bioxccl	RRID: AB_10949073
InVivoMab anti-mouse 4-1BBL (CD137L)	Bioxccl	RRID: AB_10949069
InVivoMab rat IgG2a isotype control, anti-trinitrophenol	Bioxccl	RRID: AB_1107769
InVivoMab rat IgG2b isotype control, anti-keyhole limpet hemocyanin	Bioxccl	RRID: AB_1107780
InVivoPlus anti-mouse 4-1BB (CD137)	Bioxccl	RRID: AB_10949016
Human BATF3 Antibody	R&D	RRID: AB_11127798
FLEX Monoclonal Mouse Anti-Human CD8, Clone C8/144B	Dako	RRID: AB_3073940
Human/Rat SOX10 Antibody	R&D	RRID: AB_2195180
Anti-pan Cytokeratin antibody [AE1/AE3]	abcam	RRID: AB_1640401
Biological samples		
Human tumor samples (scRNAseq data)	SadeFeldman et al. (2018) ³²	GEO: GSE120575
Human tumor samples (scRNAseq data)	Steele et al. (2020) ³¹	GEO: GSE155698
Human tumor samples (scRNAseq data)	Zhang et al. (2021) ³³	GEO: GSE169246
Human tumor samples (scRNAseq data)	Cheng et al. (2021) ¹⁰²	GSE154763
Human tumor samples (scRNAseq data)	Mulder et al. (2021) ²⁸	https://gustaveroussy.github.io/FG-Lab/
Human metastatic melanoma biopsies (FFPE)	Human tissue resource center, University of Chicago	https://voices.uchicago.edu/htrc/
Human muscle-invasive primary bladder cancer samples (FFPE)	Human tissue resource center, University of Chicago	https://voices.uchicago.edu/htrc/

(Continued on next page)

Continued

REAGENT or RESOURCE	SOURCE	IDENTIFIER
Chemicals, peptides, and recombinant proteins		
FTY720	Sigma	SML0700-25MG
Diphtheria toxin	Sigma	D0564-1MG
Collagenase IV	Sigma	C5138
DNAse type IV	Sigma	D5025
Hyaluronidase type V	Sigma	H6254
Brefeldin A	Sigma	B7651-25MG
Ficoll-Paque™ PLUS Media	Cytiva	45-001-750 (FisherScientific)
BD Horizon™ Brilliant Stain Buffer Plus	BD bioscience	566385
eBioscience™ Foxp3/Transcription Factor Staining Buffer Set	eBioscience	00-5523-00
True-Stain Monocyte Blocker™	Biolegend	426103
CountBright™ Absolute Counting Beads	Invitrogen	C36950
UltraComp eBeads™ Plus Compensation Beads	Invitrogen	01-3333-42
H-2Kb/SIY-pentamer (PE labeled)	ProlImmune	F1803-2B - 150 test R-PE
Critical commercial assays		
Visium FFPE kit	10X genomics	1000338
CytAssist Visium FFPE kit	10X genomics	1000522
Deposited data		
Raw data and code used to analyze it	This paper	GEO: GSE238145
Experimental models: Cell lines		
B16-SIY (B16F10 engineered to express dsRed in-frame with the model antigen peptide SIYRYGL)	Laboratory of Dr. Thomas Gajewski	N/A
MC38.SIY (MC38 engineered to express GFP in-frame with the model antigen peptide SIYRYGL)	Laboratory of Dr. Thomas Gajewski	N/A
Experimental models: Organisms/strains		
C57BL/6J	The Jackson Laboratory	IMSR_JAX:000664
B6.SJL-Ptprca Pepcb/BoyJ (CD45.1)	The Jackson Laboratory	IMSR_JAX:002014
B6.SJL-Ptprca/BoyAiTac (CD45.1)	Taconic	Cat# 4007-F
B6.129S6-Rag2tm1Fwa N12 (Rag2KO)	Taconic	Cat# RAGN12-F
B6.FVB-1700016L21RikTg(ltgax-HBEGF/EGFP)57Lan/J (CD11c_DTR_GFP)	The Jackson Laboratory	IMSR_JAX:004509
B6.129S(C)-Batf3tm1Kmm/J (Batf3 KO)	The Jackson Laboratory	IMSR_JAX:013755
4-1BB KO mice	Croft Lab, La Jolla institute for Immunology	https://www.lji.org/labs/croft/
Software and algorithms		
FlowJo	Tree Star	https://www.flowjo.com/
GraphPad 9 Software	Prism	https://www.graphpad.com/
inForm® Cell Analysis	Akoya	https://www.akoyabio.com/phenoimager/inform-tissue-finder/
Ripley's Multitype K-function (kcross)	N/A	https://www.rdocumentation.org/packages/spatstat.core/versions/2.3-1/topics/Kcross
Loupe Browser	10X genomics	https://www.10xgenomics.com/products/loupe-browser/downloads

(Continued on next page)

Continued

REAGENT or RESOURCE	SOURCE	IDENTIFIER
Space Ranger	10X genomics	https://support.10xgenomics.com/spatial-gene-expression/software/pipelines/latest/what-is-space-ranger
R	R Core Team	https://www.R-project.org
Seurat package	Hao, Y. et al.	https://doi.org/10.1016/j.cell.2021.04.048
Giotto package	Dries, R. et al.	https://doi.org/10.1186/s13059-021-02286-2
GSEABase package	Martin Morgan, Seth Falcon and Robert Gentleman (2021)	https://doi.org/10.18129/B9.bioc.GSEABase
Msigdbr package	Igor Dolgalev (2021)	https://CRAN.R-project.org/package=msigdbr
ClusterProfiler package	Yu, G. et al.	https://doi.org/10.1089/omi.2011.0118
ComplexHeatmap package	Gu, Z. et al.	https://doi.org/10.1093/bioinformatics/btw313

RESOURCE AVAILABILITY

Lead contact

Further information and requests for resources and reagents should be directed to and will be fulfilled by the lead contact, Thomas F. Gajewski, M.D., Ph.D. (tgajewsk@bsd.uchicago.edu).

Materials availability

This study did not generate new unique reagents.

Data and code availability

- Spatial transcriptomics data have been deposited at GEO (GEO: GSE238145) and are publicly available as of the date of publication. Accession number is listed in the key resources table. Multiplex Immunofluorescence data reported in this paper will be shared by the lead contact upon request.
- All original code has been deposited at GEO and is publicly available as of the date of publication. Accession numbers are listed in the key resources table.
- Any additional information required to reanalyze the data reported in this work paper is available from the lead contact upon request.

EXPERIMENTAL MODEL AND STUDY PARTICIPANT DETAILS

Mouse strains

C57BL/6 and B6.SJL (CD45.1) were purchased from Taconic or Jackson Laboratory. RAG2 knock-out (KO) mice were purchased from Taconic. CD11c_DTR_EGFP and Batf3 KO mice were purchased from the Jackson Laboratory, and 4-1BB KO mice were a gift from Dr. Kwon and Dr. Croft. Mice were used at 6–12 weeks of age. All mice were housed at the University of Chicago specific pathogen free facility, were maintained according to the National Institute of Health Animal Care guidelines, and studied under IACUC-approved protocols.

Cell lines

B16·SIY cells and MC38.SIY used in this work were previously generated in the Gajewski laboratory. B16F10 (ATCC) cells were engineered to express dsRed in-frame with the model antigen peptide SIYRYGYL (B16·SIY), which can be recognized by CD8⁺ T cells in the context of H2-K^b.^{18,19} MC38.SIY express GFP in-frame with the SIYRYGYL peptide.

METHOD DETAILS

Cell culture and tumor inoculation

B16·SIY and MC38.SIY cells were cultured in DMEM (Life Technologies) with 10% FBS (Atlanta Biologicals), 100 U/ml Penicillin-Streptomycin (Gibco), 1% MEM Non-Essential Amino Acids (Gibco), and 0.01 M MOPS. All cell lines were routinely tested for mycoplasma contamination using the HEKBlue (InvivoGen) reporter cell line, following the manufacturer's protocol. For inoculation, cells were washed with PBS, trypsinized with 0.05% Trypsin (Gibco) and collected with cell culture medium. Cells were washed twice with PBS and then resuspended in PBS for injection. 2x10⁶ B16·SIY cells or 1x10⁶ MC38.SIY in 100 μ L were inoculated subcutaneously into the left flank of each animal. For the mixed bone marrow chimeras, MC38.SIY tumor cells were injected on the back/side of the

mice. Tumors were measured with digital calipers starting at day seven of tumor inoculation and tumor volume (TV) was calculated as $TV = TL \times TW \times TH$, where TL is the tumor length, TH is tumor height, and TW is tumor width.

Bone marrow chimeras

CD45.1 recipient mice were irradiated with 1050 cGy total gamma radiation from a cesium-137 source. Irradiation was split into two doses, 500 cGy followed by 550 cGy 3 h later. One day after irradiation, bone marrow was harvested from donor mice. Bone marrow was isolated from the femurs and tibias by flushing bones with cold PBS through a 70 μ m mesh. Approximately 5×10^6 bone marrow cells were injected through the tail vein into previously irradiated mice. For mixed BM chimeras, BM cells from CD11c_DTR_EGFP (CD45.2) mice were mixed in a 50:50 ratio with BM cells from WT (CD45.1) or Batf3 KO (CD45.1/2) mice. Chimeric mice were rested for at least 12 weeks before being used in experiments. Percentage of chimerism was evaluated in the blood of all mice before tumor injection. FTY720 (40 μ g) was given to all mice every day from day 7 of tumor inoculation to prevent the entry of new T cells into the tumor. Also, 500 ng of Diphtheria toxin (DT) was given intraperitoneally on day 7, 8 and every other day until the end of the experiment, to all mice on the mixed BM chimeras and to the indicated groups of mice in the CD11c_DTR_EGFP chimeras. Indicated mice were treated with anti-PD-L1 or vehicle (PBS) at days 9, 12, 15 and 18 of tumor injection for B16·SIY and with anti-PD-L1 or Rat IgG2b isotype control for the MC38.SIY tumor model. Tumor growth was measure until the end of the experiment, when mice were sacrificed, and tumors were analyzed by flow cytometry for DCs and T cell infiltration.

RAG2 KO experiments

RAG2 KO mice were adoptively transferred with splenocytes from WT or 4-1BB KO mice. After 8 weeks, the percentages of T cells in all mice were analyzed and after confirming they were similar to the percentage of T cells in C57BL/6 mice, 2×10^6 B16·SIY cells were injected subcutaneously. Then, mice were treated or not with anti-PD-L1 at days 7, 10, 13 and 16 after tumor injection.

FTY720 administration

FTY720 (SIGMA) was dissolved in water and then further diluted in water before administration. Oral gavage of 40 μ g in 100 μ L of volume was given per mouse since day 7 after tumor injection and continued daily for the duration of the experiments.

Ag-specific CD8⁺ T cell functionality experiments

For functional analysis of Ag-specific CD8⁺ T cells, C57BL/6 mice were injected with B16·SIY tumor cells. After 7 days of tumor injection, FTY720 was given to all mice daily until the end of the experiment. At day 8, 11 and 14 mice were treated with or without anti-PD-L1, in the presence of anti-4-1BBL mAb or isotype control. On day 15, 100 μ L of Brefeldin A (1 mg/mL) was injected intratumorally in all mice. If tumors were big, brefeldin A was injected in two different parts of the tumor. Brefeldin A was diluted in DMSO to a 10 mg/mL solution and diluted further in PBS to get the 1 mg/mL solution. Five hours after brefeldin A injection, mice were euthanized, tumors were removed, weighed and digested as explained below, but with the addition of Brefeldin A (10 μ g/mL) in all steps until cells were fixed during the flow cytometry staining protocol.

Tumor and blood processing

In experiments that involved FTY720 treatment, retro-orbital or sub-mandibular bleeding of mice was performed at the end of the experiments to analyze FTY720 efficacy in preventing the egress of T cells into the circulation. C57BL/6 mice were also bled for no-FTY720 treatment controls. For chimeric experiments, blood was also collected after 12 weeks of bone marrow transfer, before tumor injection, for chimerism analysis. At the end of the experiments, tumors were removed, weighed and digested using an enzyme mix in RPMI (Life Technologies) containing Collagenase IV (1 mg/mL, Sigma C5138), DNase type IV (20 U/mL, Sigma: D5025), and Hyaluronidase type V (100 μ g/mL, Sigma: H6254) for 30 min at 37°C while rotating. Then, tumor suspensions were incubated on ice for 10 min and filtered through a 70 μ m mesh. After washing with cold PBS, cells were filtered for a second time and live mononuclear cells were further enriched by layering Ficoll-Hypaque gradient (GE Healthcare) beneath the cell suspension, followed by centrifugation without breaks for 30 min at 500 x g. The mononuclear cell layer was isolated, washed with PBS and stained with mAb for flow cytometry analysis.

Flow cytometry

Cells were first stained for Ag-specific (SIY⁺) CD8⁺ T cell identification with H-2Kb/SIY-pentamer (PE; ProImmune) for 20 min at room temperature at a 1:20 dilution, followed by staining with remaining antibodies for 30 min at 4°C. Staining was performed in a solution of PBS with 2% FBS, Brilliant Stain Buffer (BD) and for myeloid cell staining also with True-Stain Monocyte Blocker (Biolegend). All stainings were done in the presence of CD16/CD32 (IgG Fc receptor III and II, respectively) blocking antibodies (Biolegend). For 4-1BBL detection, anti-4-1BBL biotinylated mAb was mixed with the rest of the mAbs, and after the incubation and washing steps, a Streptavidin-PE staining (1:400 dilution) was performed for 30 min at 4°C. If intracellular staining was not performed, cells were then washed and fixed in 1% paraformaldehyde. For intracellular staining, after the surface staining was performed, cells were fixed and permeabilized using the Foxp3 staining kit (BD) according to manufacturer's protocol, then incubated overnight with the mix of intracellular mAb and washed before flow cytometer acquisition. For functional analysis of Ag-specific CD8⁺ T cells, brefeldin A (1 mg/mL) was present during all the steps of staining until the cells were fixed and permeabilized. Counting beads (countbright absolute

counting beads or the PLUS version, Invitrogen) were added to each sample before flow acquisition. Cells and/or beads (Ultracomp eBeads Plus compensation beads, Invitrogen) were used for staining of the positive/reference controls. Cells were analyzed on either a BD Fortessa or Cytex Aurora and analyzed using FlowJo software (Tree Star). Gating of the populations was done according to the Fluorescence-minus-one (FMO) tubes.

Immunotherapy and blocking antibodies

Antibodies against PD-L1 (10F.9G2), 4-1BB (LOB12.3), 4-1BBL (TKS-1), Rat IgG2a (2A3) and Rat IgG2b (LTF-2) were purchased from Bio X Cell (West Lebanon, NH). Antibodies were diluted in PBS and 100 μ g of anti-PD-L1, 100 μ g of anti-4-1BB, 100 μ g of Rat IgG2b (as anti-PD-L1 isotype control when using the MC38.SIY tumor model) and 250 μ g of anti-4-1BBL or Rat IgG2a as isotype control, were given per treatment per mouse. Antibodies were administered intraperitoneally. Immunotherapy was given every 3 days for 3 or 4 total doses (as indicated in figure legends), starting at day 9 after tumor inoculation for chimeric experiments, starting at day 8 for other experiments involving FTY720 treatment, and starting at day 7 for the rest of the experiments.

scRNAseq analysis for selection of the DC1 marker to be used in the multiplex immunofluorescence staining

Mulder et al. expression analysis:

We visualized the expression of XCR1, CLEC9A, BATF3, and THBD from Mulder et al. 2021 with the VlnPlot function from Seurat, with expression grouped by the cluster annotations provided by the authors.

Gene Co-expression in scRNA data:

We examined five prior studies (summarized in table below) for expression of XCR1, CLEC9A, BATF3, THBD, ITGAX, and HLA-DRA. In each case, the published data were obtained from GEO and imported into R using Seurat. We then summed the number of cells in each dataset that expressed each combination of these genes.

Study	GEO Accession
SadeFeldman et al. 2018	GEO: GSE120575
Steele et al. 2020	GEO: GSE155698
Zhang et al. 2021	GEO: GSE169246
Cheng et al. 2021	GEO: GSE154763
Mulder et al. 2021	*

*Mulder et al. data obtained directly from lab GitHub repository for MNP_Verse: <https://gustaveroussy.github.io/FG-Lab/>

Multiplex Immunofluorescence staining

Multiplex immunohistochemistry was applied to pre-treatment biopsy samples from a total of 41 advanced melanoma patients and to 41 surgically resected muscle-invasive human primary bladder cancer samples. The antibody panel consisted of Batf3 (polyclonal [AF7437], R&D Systems, Minneapolis, MN, USA), CD8 (clone C8/144B, Dako, Santa Clara, CA, USA), and SOX10 (clone 20B7, R&D Systems, for the melanoma samples) and pan-cytokeratin (clone AE1/AE3, Abcam, for the bladder samples). 5- μ m cut sections from formalin-fixed paraffin embedded (FFPE) blocks were stained using Opal multiplex kit (AKOYA Bioscience, Menlo Park, CA, USA) according to the manufacturer's instruction. Briefly, slides were baked for 1 h at 60°C. After deparaffinization and rehydration, tissues were fixed with 10% neutral buffered formalin. Antigen retrieval was performed with pH9 buffer for 20 min at 110°C in a pressure cooker followed by blocking. Tissues were then incubated with each primary antibody for 1 h at room temperature followed by a horseradish peroxidase-conjugated secondary antibody for 10 min at room temperature. Signal improvement was achieved by tyramide signal amplification with the corresponding Opal fluorophore (AKOYA Bioscience, Menlo Park, CA, USA) in a 10 min reaction at room temperature. The process from antigen retrieval to signal amplification was repeated for each of the target molecules. After staining all the target molecules, slides were counterstained with 4', 6-diamidino-2-phenylindole (DAPI) and were mounted and cover slipped.

Multispectral scanning

The stained slides were imaged using the Vectra Polaris Automated Quantitative Pathology Imaging System (AKOYA Bioscience, Menlo Park, CA, USA) at 20x resolutions with the following channels: DAPI, FITC, Cy3, Texas red and Cy5. On each scanned image, up to five regions of interest (ROIs) with the preset size of 931 μ m x 698 μ m that had the most abundant CD8⁺ cell infiltration was selected in tumor nests. Those selected ROIs were scanned at 20x resolutions to make .im3 format image files for the following image analysis.

Image analysis

The scanned .im3 format image files were analyzed using inForm Cell Analysis software (AKOYA Bioscience, Menlo Park, CA, USA). Tissue segmentation was performed by highlighting examples of SOX10⁺ tumor area, SOX10⁺ stromal area, and non-cellular area, and allowing the algorithm to learn each tissue sub-region. Cell segmentation was performed using DAPI counterstain, and x and y position was assigned to each cell. The following cell phenotypes were determined by highlighting examples of each cell phenotype

and allowing the algorithm to learn each cell phenotype: SOX10⁺ (or pancytokeratin⁺ for bladder samples) CD8⁺, Batf3⁺, and others. Finally, batch analysis using the trained algorithm was performed for all the ROIs, outputting information including tissue area and phenotype of each cell. The numbers of each immune cell phenotype were calculated as the numbers in a specific ROI divided by the number of the total cells in that ROI. Then, the CD8⁺ cells from all the ROIs were added up to give the number of CD8⁺ cells of each patient. The same was done to calculate the number of Batf3⁺ cells of each patient. To assess whether the number of Batf3⁺ DCs and CD8⁺ T cells was associated with clinical response to anti-PD-1, we analyzed the numbers of each cell type and the objective responses to treatment of each melanoma patient. Clinical response was available for 36 out of the 41 patients and was determined by using Response Evaluation Criteria In Solid Tumors (RECIST, version 1.1). These data was used for the correlation analysis and also for z-scores analysis. For this, the data was normalized by calculating the z-scores as follow: $z = (x - \mu) / \sigma$, where x is the number of that specific type of cell for that patient, μ is the mean of that type of cell for all patients, and σ is the standard deviation for that type of cell for all patients. The K AUC high and K AUC low groups of patients were split according to the median, and then the objective response rate (ORR) was calculated.

Immunofluorescence spatial analysis

After setting up criteria that assigned each cell to a certain phenotype, all datasets (regions of interest from each slide, ROIs) that didn't have at least one Batf3⁺ and two CD8⁺ cells were filtered out from the list of datasets to be analyzed. A total of 39 patients were included in the analysis as they had at least one region of interest with at least one Batf3⁺ cell and two CD8⁺ cells. Then, for each dataset we created a temporary matrix with only the Batf3⁺ and CD8⁺ cells, standardized the x and y positions to between 0 and 1 so that the maximum distance between two cells is 1, then we converted it into point pattern object (ppp). Next, we ran the ppp using the modified Ripley's Multitype K-function (kcross), with the edge correction "best" and 2000 points (r). Results from all the ROIs for each patient were averaged to have one result per patient. A plot was created showing all individual patient curves, which shows the result of the K function " $K(r)$ " at each distance " r ", and the expected theoretical curve for a random distribution of cells, with the 95% confidence interval shown in gray. Another plot was created with the merge of the patient curves and the theoretical curve for a random distribution, with the 95% confidence interval shown in gray. To create the confidence intervals for the theoretical random distribution curve, we performed Monte Carlo simulations for each patient slide by generating 99 Kcross functions with Batf3⁺ and CD8⁺ cells being randomly distributed and calculating the confidence interval for those 99 Kcross functions. Then, we averaged the mean of the lower and the upper bounds of the confidence intervals of all the patients to get the general upper and lower values of the confidence interval of the theoretical curve. In addition, the area under the curve (AUC) for each individual curve and for the theoretical curve were calculated and a one sample t test was performed to analyze the statistical difference between them. Of note, the Ripley's Kcross-function is telling the number of CD8⁺ cells within certain distance from Batf3⁺ cells, normalizing by the CD8⁺ cell density.

Spatial transcriptomics

Spatial transcriptomic analysis (10x Genomics CytAssist Visium FFPE kit, catalog no. 1000522, except for patient 1 which was performed with Visium FFPE kit, catalog no. 1000338, without CytAssist) was performed on archived formalin-fixed paraffin-embedded (FFPE) tissue sections from muscle-invasive human bladder carcinoma tumor samples. Spatial transcriptomics was performed according to manufacturer protocol. Briefly, tissue RNAs were isolated using Allprep DNA/RNA FFPE kit (Qiagen, catalog no. # 80234) and quality controlled (DV200 \geq 50%). Then, 5 μ m tissue sections were cut and placed onto charged slides (Fisherbrand Superfrost Plus) and dry at 42 Celsius degrees for 3 h. After keeping the slide with desiccant overnight, slides were dried again for 2 h at 60°C. Then, they were deparaffinized and covered in hematoxylin (Millipore Sigma, catalog no. MHS16) for 3 min at room temperature. After intermittent washing steps, they were covered in Bluing reagent (Agilent, catalog no. CS70203-2) and later Eosin (Millipore Sigma, catalog no. HT110116). Hematoxylin and eosin (H&E)-stained slides were imaged on a Evos M7000 Microscope. Then, probe hybridization, probe ligation, probe release, extension, elution and library construction were done according to manufacturer's protocol. The spatial transcriptome library was prepared following the manufacturer's instruction and sequenced on the NovaSeq 6000 system at the University of Chicago Genomics core facility.

Then, samples were processed following guidelines from 10X Genomics, using the Loupe Browser (<https://www.10xgenomics.com/products/loupe-browser/downloads>) for manual image alignment and Space Ranger (<https://support.10xgenomics.com/spatial-gene-expression/software/pipelines/latest/what-is-space-ranger>) to retrieve count data from the raw sequence files. All data analyses were carried out in R (R Core Team (2021) R: A Language and Environment for Statistical Computing, R Foundation for Statistical Computing, Vienna <https://www.R-project.org>) using tools from the Seurat package⁹¹ unless noted otherwise. To account for variation in cell densities in CD8⁺ spots, the raw count data were normalized by the expression of CD8A (or CD8B when CD8A not found) prior to differential expression and pathway analyses. For Figure 6B and as we were interested in the expression levels of chemokines that recruit DCs and CD8⁺ T cells in the spots that we were comparing, data were not normalized to CD8 transcripts. Each spot in Visium data is expected to include 1–10 cells, and there is an interspace between spots where DC1s and CD8⁺ cells from neighbor spots could have been interacting in the original tissue. To account for this, we first identified all spots with any DC1s marker expression (BATF3, XCR1, or CLEC9A and CD11c) or CD8 expression (CD8A or CD8B and at least one of CD3D, CD3E, or CD3G). Of note, probes for HLA genes are not included in the CytAssist kits, and therefore MHCII was not included to identify DC1s spots. We then used the function findNetworkNeighbors from the package Giotto⁹² to identify spots at different distances from DC1⁺

spots. In differential expression and pathway analyses, we defined CD8⁺ spots within or neighboring DC1⁺ spots as CD8⁺DC1s⁺ (CD8⁺ T cell in close proximity to a DC1, dark and light green spots on Figure 6A). To ensure that CD8⁺DC1s[−] spots were truly CD8⁺ T cells distant from a DC1, and because in our clustering analysis (Figure 5) we observed a non-random distribution of these two cell types in a region of approximately two and a half spots, we only considered CD8⁺DC1s[−] spots if 3 spots away from a DC1s⁺ spot (yellow spots on Figure 6A). The signatures for dysfunctional/exhausted,^{26,33–42} stem-like/progenitor^{26,42–46} and effector^{26,33–41,43–46} CD8⁺ T cells were built with genes that were part of the signatures reported in at least two other studies on human tumor samples.

Pathway analysis

GSEA⁹³ pathway analysis was carried out using the packages GSEABase (Martin Morgan, Seth Falcon and Robert Gentleman (2021). GSEABase: Gene set enrichment data structures and methods. R package version 1.54.0), msigdb (Igor Dolgalev (2021). msigdb: MSigDB Gene Sets for Multiple Organisms in a Tidy Data Format. R package version 7.4.1. <https://CRAN.R-project.org/package=msigdb>), and clusterProfiler.⁹⁴ Prior to running GSEA, we first built a pseudobulk model of the data, creating separate CD8⁺DC1⁺ and CD8⁺DC1[−] subsamples from each original tissue by summing the expression of each gene across the corresponding spots. We then processed the pseudobulk samples following standard bulk RNAseq methods with the package edgeR. This included filtering to remove genes with low expression (with the function filterByExpr) and TMM-normalizing the results using calcNormFactors, as well as converting to log2-cpm values (with the function cpm). The processed data were then analyzed with limma-voom to obtain a summary of log2-fold-change when comparing CD8⁺DC1⁺ to CD8⁺DC1[−] spots. We then sorted the resulting list of genes in descending order by the average log2-fold-change in expression within the CD8⁺DC1s⁺ spots relative to the CD8⁺DC1s[−] spots. This sorted list was then passed to the GSEA function and compared against the MSigDB Hallmark and Gene Ontology (GO) gene set collections, including Biological Processes (GO_BP), Cellular Components (GO_CC), and Molecular Functions (GO_MF). A selection of several relevant significant pathways is shown in Figure 6C, ordered by ascendent net enrichment score (NES). Of note, GSEA analysis for DC1s (Figure 6C top) was done considering spots to be CD8⁺DC1s⁺ if they expressed markers for both CD8⁺ T cells and DC1s (dark green spots on Figure 6A), and for T cell analysis (Figure 6C bottom) considering spots to be CD8⁺DC1s⁺ if CD8⁺ T cells markers were expressed in the same spot as DC1s or next to a DC1⁺ spot (dark green and light green spots on Figure 6A).

Mean expression heatmaps

To visualize the key differences between CD8⁺ T cells that are close to DC1s (CD8⁺DC1s⁺) and the ones that are distant to DC1s spots (CD8⁺DC1s[−]) for the T cell signatures (Figure 7), we log-normalized and scaled the data within each sample (considering all the CD8⁺ spots) using Seurat's NormalizeData and ScaleData functions. We then estimated the mean scaled expression for genes of interest within the CD8⁺DC1s⁺ and CD8⁺DC1s[−] spots. Results were visualized using the package ComplexHeatmap.⁹⁵ Of note, CD8⁺ T cells were considered to be close to DC1s if they were in the same spot or next to a DC1⁺ spot (dark green and light green spots on Figure 6A), and were considered to be distant to DC1s if they were at least 3 spots away from a DC1⁺ spot (yellow spots on Figure 6A). For the expression of chemokines that would explain the co-localization of DC1s and CD8⁺ cells (Figure 6B), data from spots where both DC1s and CD8 markers were present were considered as CD8⁺DC1s⁺ for the analysis (dark green spots on Figure 6A), and data was not normalized to CD8 expression. Patients with very few DC1⁺CD8⁺ spots were excluded from the analysis. Then, we log-normalized and scaled the data within each sample using Seurat's NormalizeData and ScaleData functions and estimated the mean scaled expression for genes of interest within the CD8⁺DC1s⁺ and CD8⁺DC1s[−] spots. For better understanding/visualization, results were ordered showing the CD8⁺DC1s[−] spots from all patients on the left and the CD8⁺DC1s⁺ results on the right.

QUANTIFICATION AND STATISTICAL ANALYSIS

When comparing tumor growth curves, a two-way ANOVA with Tukey's multiple comparison post-test was performed. When comparing more than two groups a one-way ANOVA with Bonferroni's post-test was used, unless the comparison was made against one control group, in which case a Dunnett's post-test was used. Outliers were removed using GraphPad Prism, with the ROUT method with a Q = 0.1%. For the spatial analysis, a one sample t test was used to compare the patients K AUC values to the K AUC value of the theoretical curve for a random distribution of cells. A Spearman's rank correlation coefficient R was used for measuring statistical dependence between the abundance of CD8⁺ cells and Batf3⁺ cells in human melanoma and bladder cancer samples. A Fisher's test was performed to compare disease control rates in the group of patients with high or low numbers of CD8⁺ and high or low number of Batf3⁺ cells. A Chi² test was used to compare the objective response rate (ORR) in the group of patients with high K AUC values to the ones with low K AUC values. All statistical analysis were performed as indicated in the figure legends, and n represents the number of mice after removal of outliers. GraphPad Prism 9 was used to compute all statistical tests. Data represent mean ± SEM. p values <0.05 were considered statistically significant and denoted as follows: *p < 0.05, **p < 0.01, ***p < 0.001, ****p < 0.0001.

Supplemental information

**Batf3⁺ DCs and the 4-1BB/4-1BBL axis
are required at the effector phase in the tumor
microenvironment for PD-1/PD-L1 blockade efficacy**

Andrea Ziblat, Brendan L. Horton, Emily F. Higgs, Ken Hatogai, Anna Martinez, Jason W. Shapiro, Danny E.C. Kim, YuanYuan Zha, Randy F. Sweis, and Thomas F. Gajewski

Supplementary Figure 1 - Ziblat A. et al

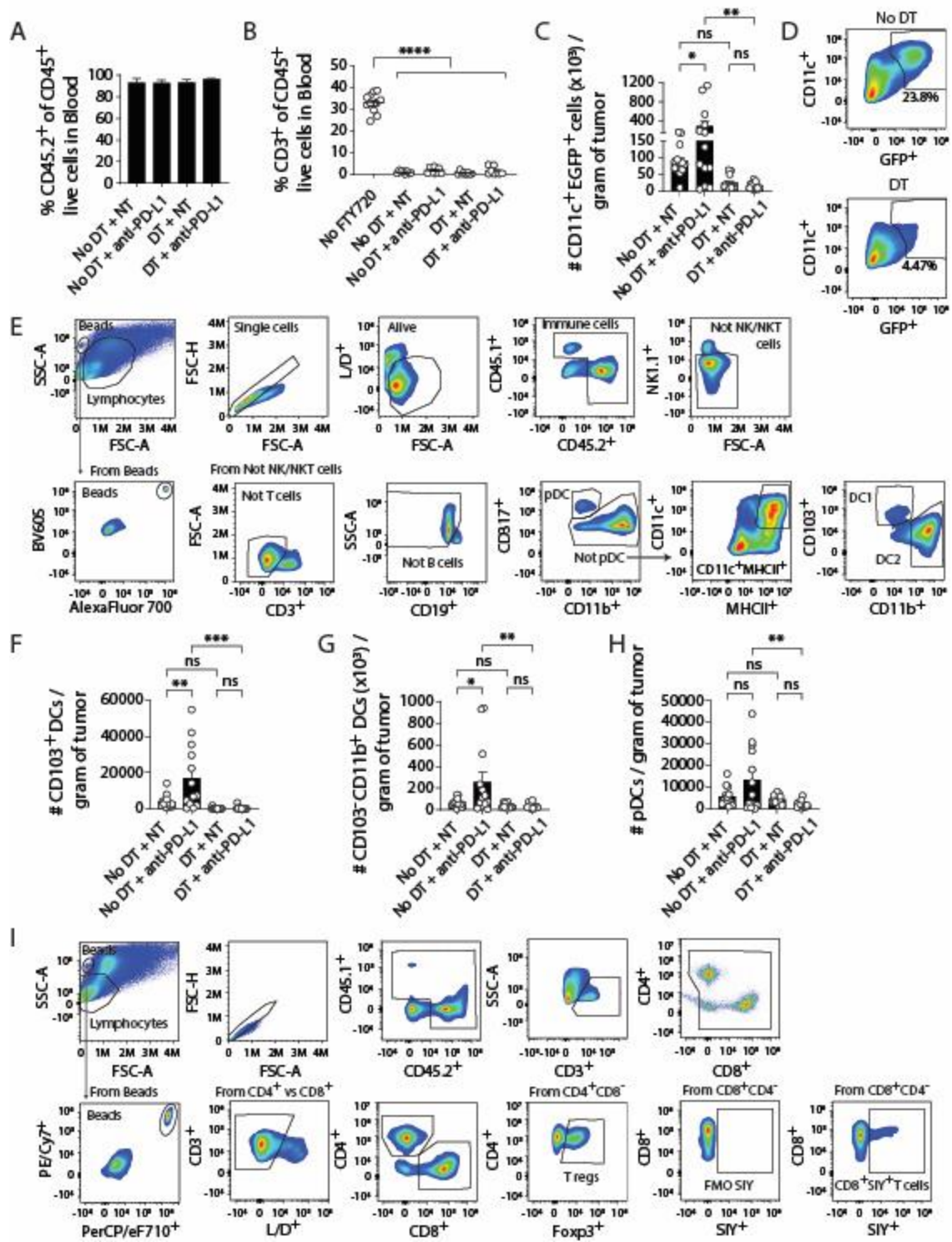


Fig. S1. Experimental design, experimental controls and flow cytometry gating strategies used for the chimeric experiments, related to Figure 1. (A) Percentage of chimerism analyzed in the blood of all mice before tumor injection. (B) FTY720 efficacy evaluated by analyzing the percentage of CD3⁺ T cells in blood in each group at endpoint, one of two independent experiments is shown, n≥8 per group. (C) DT efficacy analysis counting the number of CD11c⁺EGFP⁺ cells per gram of tumor in each group. (D) Representative flow cytometry dot plots showing CD11c⁺EGFP⁺ cells without (top panel, NT) and with DT treatment (bottom panel, DT). (E) Representative flow cytometry gating strategy used to analyze the number of pDC, DC2s and DC1s in the TME. (F-H) Number of DC1s (F), DC2s (G) and pDC (H) per gram of tumor in the TME at the end of the experiment. Two independent experiments, n=13 per group (A, C, F-H). (I) Representative flow cytometry gating strategy used to analyze the number of T cells in the TME. The gate to count the number of beads was done with different fluorophores in the axes in different experiments, selecting in each case the fluorophores that gave the best visualization/separation of the beads. Bar graphs represent the mean values of the indicated data points, and the error bars represent SEM. ns, not significant; *, p<0.05; **, p<0.01; ***, p<0.001; ****, p<0.0001. One-way ANOVA with Dunnett's post-test using "No FTY720" as control group (B) and One-way ANOVA with Bonferroni's post-test (A, C, F-H) were used for statistical analysis.

Figure S2 - Ziblat A. et al

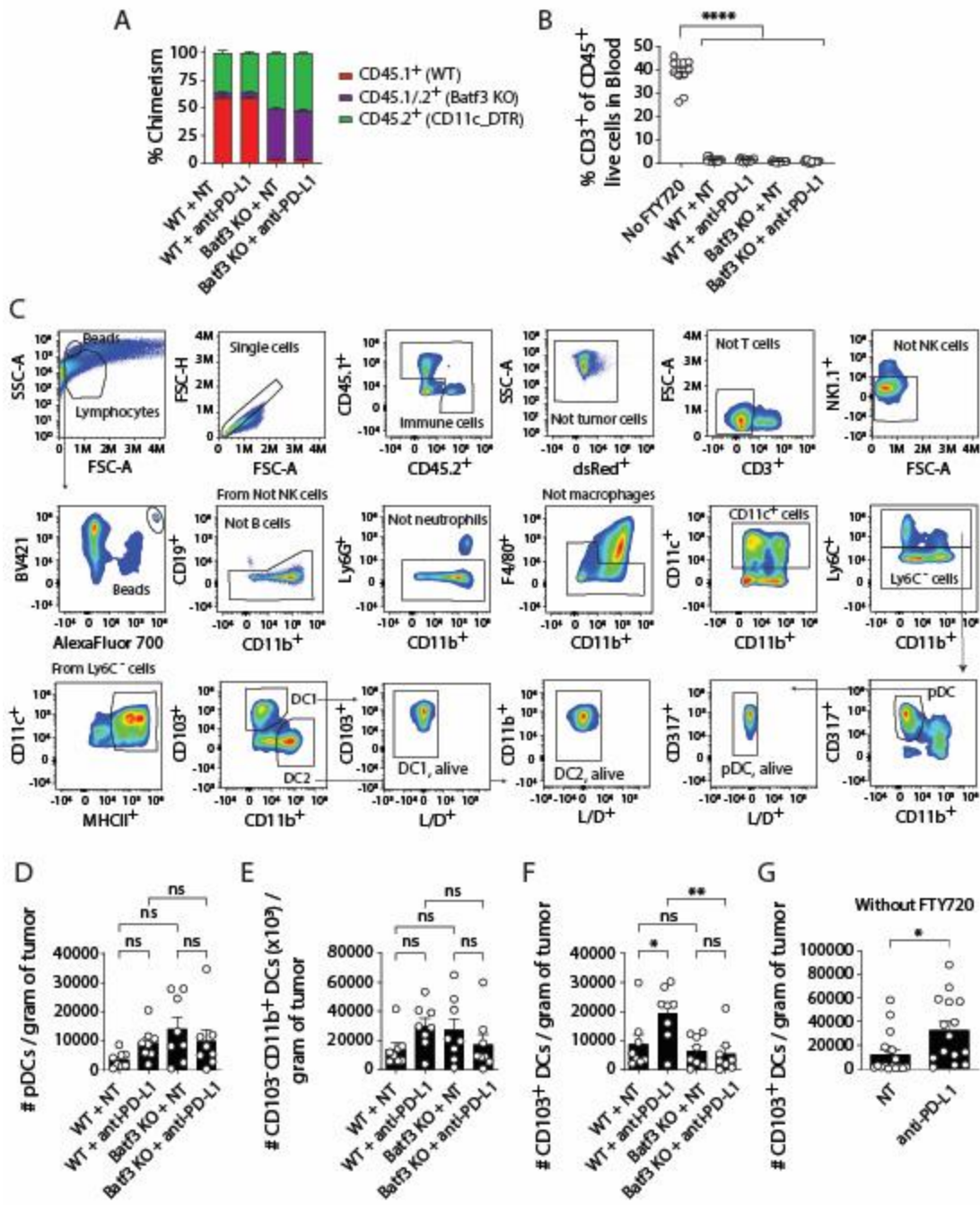


Fig. S2. Experimental controls and flow cytometry gating strategy used for the mixed BM chimera experiments, related to Figure 2. (A) Percentage of chimerism analyzed in the blood of all mice before tumor injection. Two independent experiments, $n \geq 15$ per group. (B) FTY720 efficacy evaluated by analyzing the percentage of CD3⁺ T cells in blood in each chimeric group at endpoint. Two independent experiments, $n \geq 15$ per group. (C) Representative flow cytometry gating strategy used to analyze the number of pDC, DC1s and DC2s in the tumors. (D-F) Number of pDC (D), DC2s (E), DC1s (F) per gram of tumor in each group. One of three independent experiments is shown, $n=8$ per group. (G) Number of DC1s per gram of tumor at day 24, from B6 mice injected with B16.SIY with or without anti-PD-L1 treatment, and without FTY720 treatment. Bar graphs represent the mean values of the indicated data points, and the error bars represent SEM. ns, not significant; *, $p < 0.05$; **, $p < 0.01$; ****, $p < 0.0001$. One-way ANOVA with Dunnett's post-test using "No FTY720" as control group (B), One-way ANOVA with Bonferroni's post-test (D-F) and *t*-test (G) were used for statistical analysis.

Supplementary Figure 3 - Ziblat A. et al

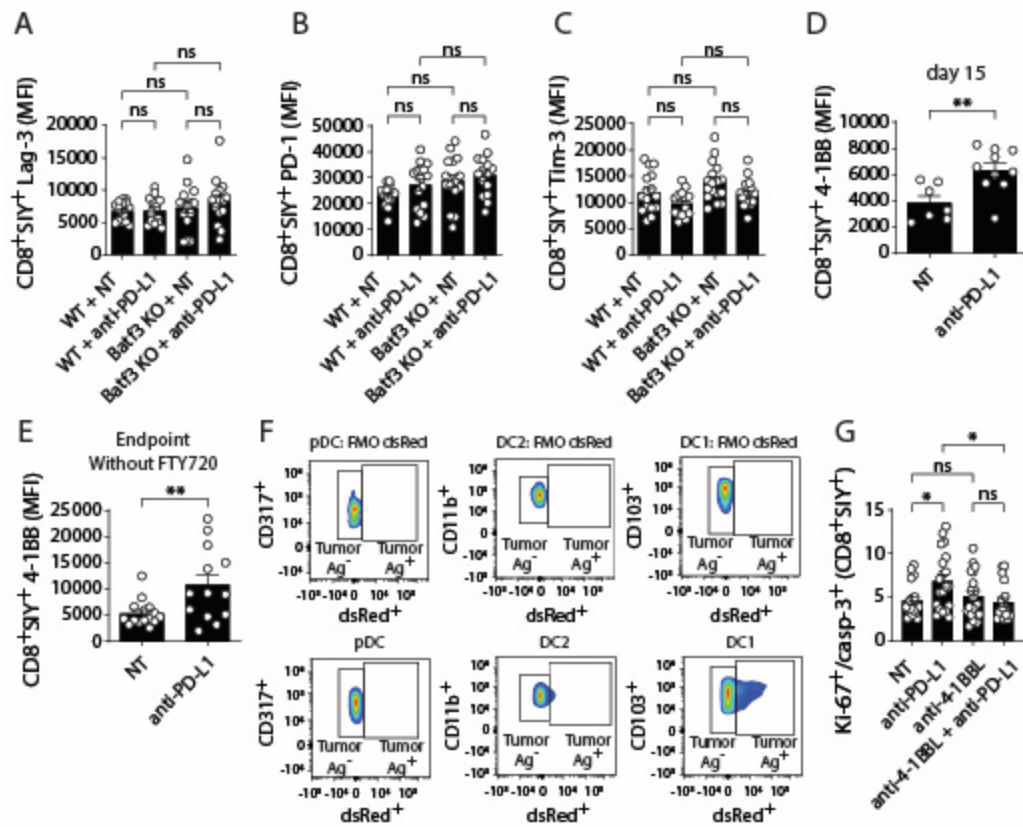


Fig. S3. Expression levels of LAG-3, PD-1 and Tim-3 on Ag-specific CD8⁺ T cells in the presence or absence of Batf3⁺ DCs, 4-1BB expression upon anti-PD-L1 treatment at different time points, gating strategy used for detection of tumor-derived material acquisition by DCs and Ag-specific CD8⁺ T cell proliferation to apoptotic ratio in different conditions, related to Figure 3. (A-C) Lag-3 (A), PD-1 (B) and Tim-3 (C) expression on Ag-specific CD8⁺ T cells in the presence or absence of Batf3⁺ DCs, with or without anti-PD-L1 treatment. Experimental design is shown in Figure 2A and gating strategy on S1I. Chimeric mice were injected with B16.SIY (A and B) or with MC38.SIY (C). Two independent experiments, n=16 per group (A and B) and n≥14 (C). (D-E) 4-1BB expression on Ag-specific CD8⁺ T cells at day 15 of tumor injection on B6 mice treated with FTY720 from day 7 of tumor injection (D) or in B6 mice at day 21 of tumor injection without FTY720 treatment (E). (F) Fluorescence minus one (FMO) for dsRed, performed by injecting mice with B16F10 (the parental tumor cell line which does not express dsRed) and representative plots of dsRed expression on pDC, DC1s and DC2s at day 9 of tumor injection, one day after one dose of anti-PD-L1 treatment. (G) Ag-specific CD8⁺ T cell proliferation (Ki-67⁺) to apoptotic (active-casp-3⁺) ratio at day 15, in mice treated with FTY720 from day 7 of tumor injection and treated with 3 doses of anti-PD-L1 in the absence or presence of anti-4-1BBL blocking mAb. Three independent experiments, n≥18. Bar graphs represent the mean values of the indicated data points, and the error bars represent SEM. ns, not significant; *, p<0.05; **, p<0.01. One-way ANOVA with Bonferroni's post-test (A-C and G), and *t*-test (D and E) were used for statistical analysis.

Supplementary Figure 4 - Ziblat A. et al

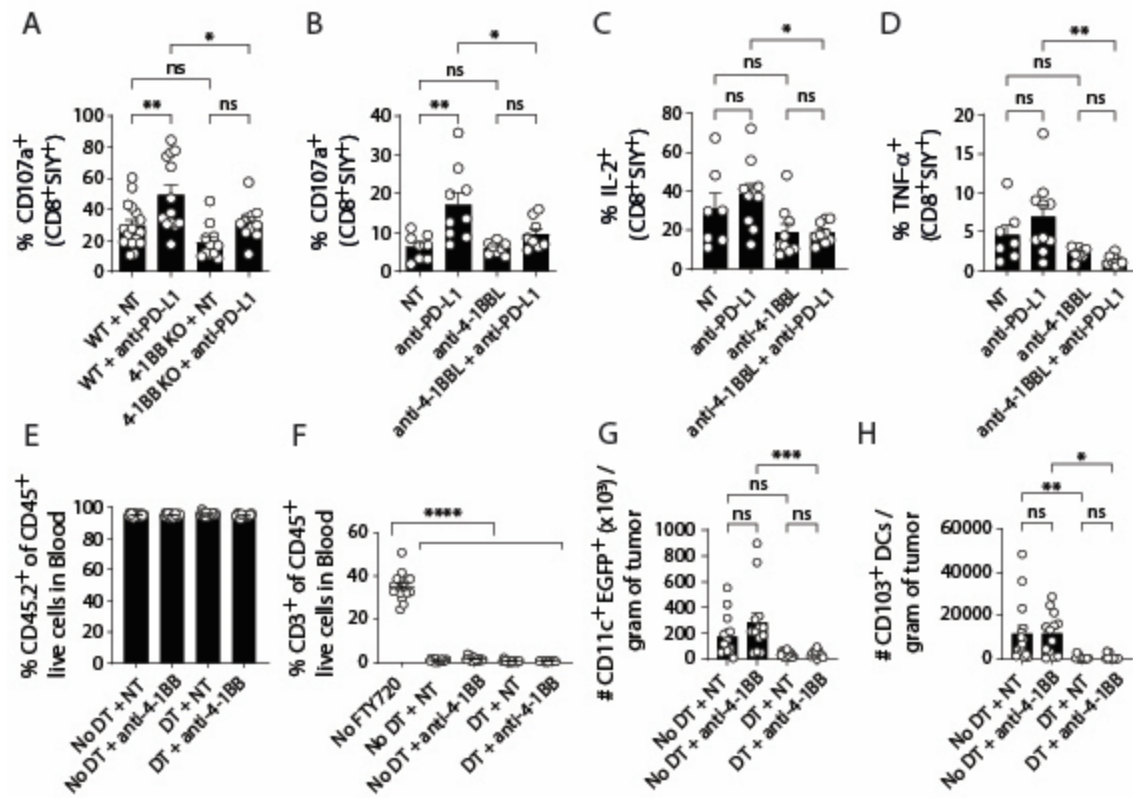


Fig. S4. 4-1BB/4-1BBL axis is needed for Ag-specific CD8⁺ T cell functional reinvigoration and controls related to Figure 4. (A) Percentage of Ag-specific CD8⁺ T cells that degranulated at day 21 of B16.SIY tumor injection in WT or 4-1BB KO mice, with or without anti-PD-L1 treatment. Two independent experiments, n≥10 per group. (B) Percentage of Ag-specific CD8⁺ T cells that degranulated at day 15 of MC38.SIY tumor injection in B6 mice, with or without anti-PD-L1 treatment in the absence or presence of anti-4-1BBL blocking mAb and treated with FTY720 from day 7 of tumor injection. One independent experiment, n≥8 per group. (C-D) Percentage of Ag-specific CD8⁺ T cells (CD8⁺SIY⁺) that expressed IL-2 (C) or TNF-α (D) in the TME at day 15 after B16.SIY tumor injection, in each group of mice. Experimental design depicted on Figure 4A. One independent experiment, n≥7. (E) Percentage of chimerism analyzed in the blood of all chimeric mice before tumor injection. Two independent experiments, n≥12 per group. (F) FTY720 efficacy in the chimeric mice evaluated by analyzing the percentage of CD3⁺ T cells in blood in each group at endpoint. Two independent experiments, n≥12 per group. (G) DT efficacy analysis counting the number of CD11c⁺EGFP⁺ cells per gram of tumor in each group. Two independent experiments, n≥12 per group. (H) Number of CD103⁺ DCs per gram of tumor in the chimeric mice treated or not with diphtheria toxin (DT) and treated or not with anti-4-1BB agonistic mAb. Bar graphs represent the mean values of the indicated data points, and the error bars represent SEM. ns, not significant; *, p<0.05; **, p<0.01; ***, p<0.001; ****, p<0.0001. One-way ANOVA with Bonferroni's post-test (A-E, G and H) and with Dunnett's post-test using "No FTY720" as the control group (F) were used for statistical analysis.

Supplementary Figure 5 - Ziblat A. et al

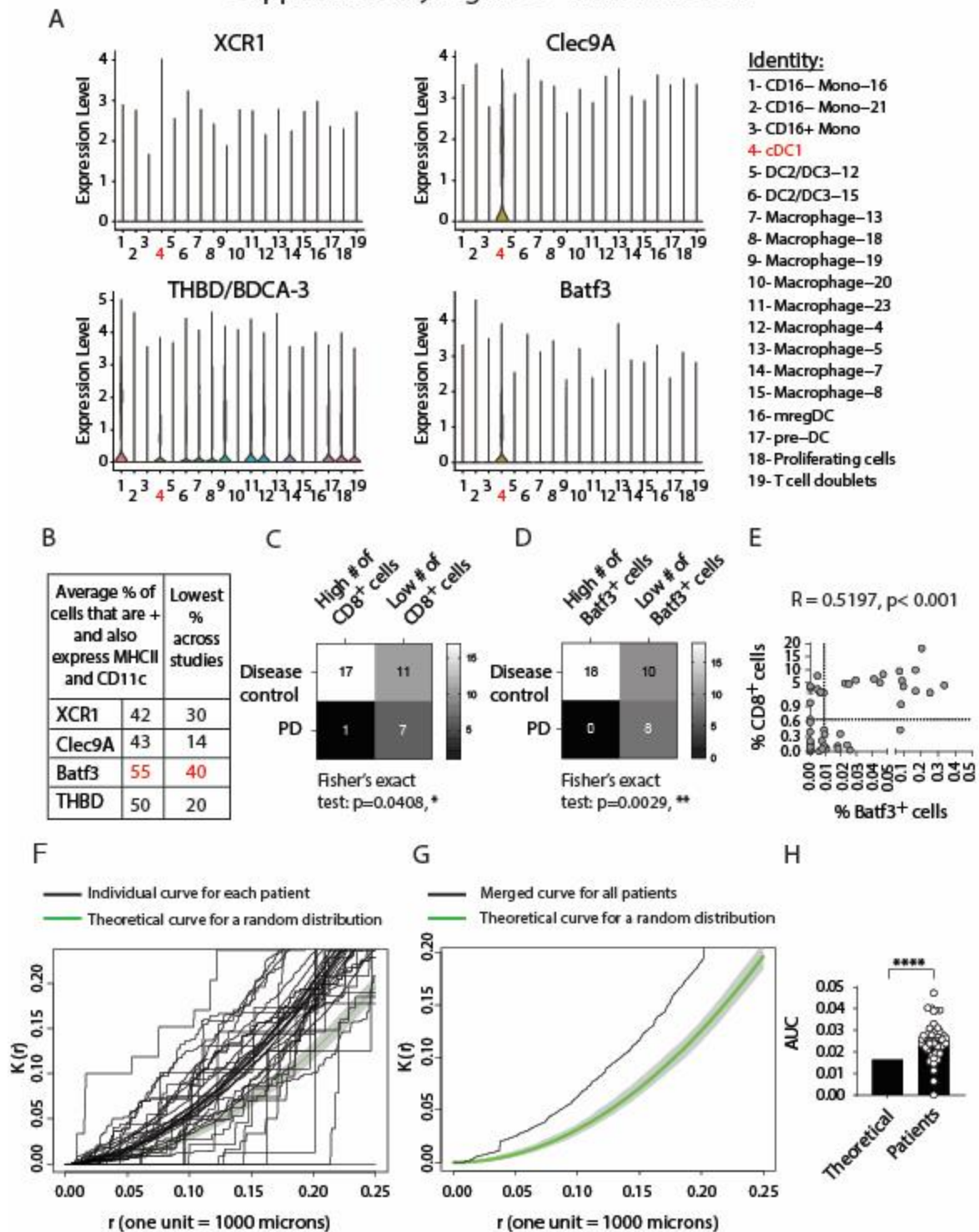


Fig. S5. Selection of the best gene to identify DC1s in human tumor samples, melanoma patients with higher number of CD8⁺ and Batf3⁺ cells have a higher disease control rate, and there is a correlation between the number of CD8⁺ and Batf3⁺ cells and these cells are clustering in primary bladder cancer samples, related to Figure 5. (A) Violin plots showing the expression of DC1 markers (XCR1, Clec9a, BDCA-3/THBD and Batf3) on different myeloid populations. Analysis performed on scRNAseq data from Mulder *et al*²⁸. (B) Average percentage of cells that are positive for the DC1 marker and simultaneously express MHCII and CD11c genes (left column) and lowest percentage of cells that express the DC1 gene and MHCII and CD11c, across all the data sets analyzed (right column). Analysis performed on scRNAseq data from several public data^{28,31–33,102}. (C, D) Heat map representation of the number of patients with high or low number of CD8⁺ cells (C) or Batf3⁺ cells (D) in melanoma and their clinical response to checkpoint blockade. (E) Correlation between the number of CD8⁺ cells and Batf3⁺ cells in 47 samples of human bladder cancer. Each dot on the graph represents one patient and shows the number of each cell type. Dotted lines indicate the median for each cell type. (F) Spatial analysis of the mIF images with the Kcross function that measures the number of CD8⁺ cells within certain distance from Batf3⁺ cells, normalizing by CD8⁺ cells density. Each black curve represents an individual patient, and the green curve indicates the theoretical curve based on a random distribution of cells. Gray area indicates the confidence interval of the theoretical curve. Curves above the upper border of the confidence interval of the theoretical curve for a random distribution indicate CD8⁺ cells and Batf3⁺ cells aggregation/clustering. A total of 41 patients were included in the analysis as they had at least one region of interest with at least one Batf3⁺ cell and two CD8⁺ cells. (G) Spatial analysis where the black line represents the merged curve for all patients and the green line is the theoretical curve for a random distribution of the cells, with the confidence interval in gray. (H) Comparison of the patient's area under the curve (AUC) and the AUC from the theoretical curve. A Fisher's exact test was used for the comparison of the disease control rate in high and low CD8⁺ cell and Batf3⁺ cell numbers groups (C and D), a Spearman's correlation was used to analyze the correlation between CD8⁺ cells and Batf3⁺ cells percentages (E) and a one sample *t*-test was used for the comparison of AUC (H). *, *p*<0.05; **, *p*<0.01; ***, *p*<0.001; ****, *p*<0.0001.

Supplementary Figure 6 - Ziblat A. et al

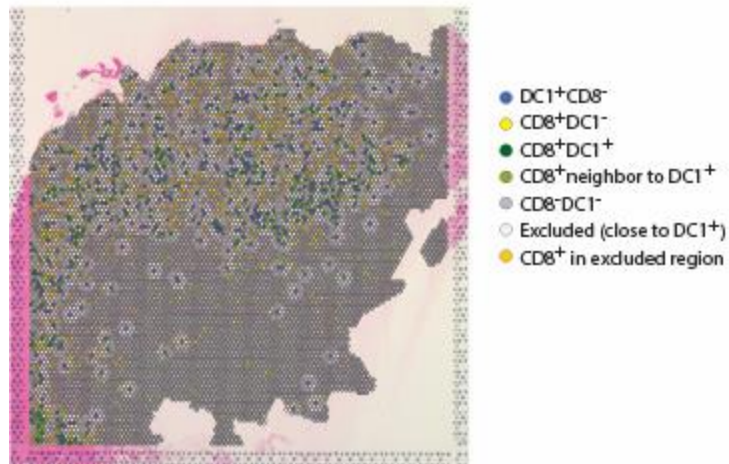


Fig. S6. Strategy used for spatial transcriptomics analysis of human bladder tumor samples, related to Figure 6. Representative image showing the spatial distribution of the Visium spots colored differentially according to the presence/absence of CD8⁺ T cell and DC1 gene markers. In grey, spots that do not express either of the markers. In dark green, spots which express both, CD8⁺ T cell and DC1 markers. In light green, CD8⁺ spots that are next to a DC1⁺ spot. In blue, DC1⁺CD8⁻ spots. In white, spots within 2 spots from a DC1s⁺ spot. In yellow, CD8⁺DC1s⁻ spots, considered distant from DC1s (at least 3 spots from any DC1⁺ spot). In orange CD8⁺ spots that were removed from the analysis for being not distant enough nor close enough to DC1s.